Research Square

Preprints are preliminary reports that have not undergone peer review.
They should not be considered conclusive, used to inform clinical practice,
or referenced by the media as validated information.

The combined influence of Al2 O3 and TiO2 nano-additives on performance, emission, and combustion of CI engines using castor biodiesel blend

Yordanos Geremew Chernet
Addis Ababa Science and Technology University
Samson Mekbib Atnaw
samson.mekbib@aastu.edu.et
Addis Ababa Science and Technology University
Adem Siraj Mohammed
Addis Ababa Science and Technology University

Research Article

Keywords: Castor, biodiesel, Nanoparticle, Oxidation stability, performance, Emission Performance, Combustion

Posted Date: June 24th, 2026

DOI: https://doi.org/10.21203/rs.3.rs-9900393/v1

License: This work is licensed under a Creative Commons Attribution 4.0 International License.
Read Full License

Additional Declarations: No competing interests reported.

The combined influence of Al_2O_3 and TiO_2 nano-additives on performance, emission, and combustion of CI engines using castor biodiesel blend

Yordanos Geremew Chernet[1, 2], Samson Mekbib Atnaw[1, 2 *], Adem Siraj Mohammed[1, 2]

[1] Department of Mechanical Engineering, College of Engineering, Addis Ababa Science and Technology University, P.O. Box 16417, Addis Ababa, Ethiopia;
[2] Sustainable Energy Center of Excellence, Addis Ababa Science and Technology University, P.O. Box 16417, Addis Ababa, Ethiopia

*samson.mekbib@aastu.edu.et

Abstract

The increasing environmental and economic concerns associated with fossil fuel consumption have driven the search for sustainable alternatives in internal combustion (IC) engines. This study investigates castor biodiesel, a renewable Ethiopian resource, enhanced with aluminum oxide (Al_2O_3) and titanium dioxide (TiO_2) nanoparticles for use in compression ignition engines. Biodiesel was produced via transesterification, and nano-additives (20–50 ppm) were dispersed using sonication and surfactants. Tests at 2700 rpm under 0–80% load evaluated physicochemical properties, engine performance (BTE, BSFC, CP, HRR), and emissions (CO, HC, NO_x). Results indicated that TiO_2 and Al_2O_3 nanoparticles improved combustion behavior and engine efficiency, with B20 blends showing increases in HRR by 5.0% and 3.8%, respectively. The hybrid blend (B20A20T20) further enhanced BTE by up to 10.3% and reduced BSFC by 13.9% compared to base B20. While biodiesel blends significantly reduced CO and HC emissions due to improved oxidation, they also increased NO_x by up to 116%, a drawback exacerbated by nanoparticle addition, with NO_x and CO emissions rising by 241.5% and 170.3%, respectively. Despite these emission trade-offs, the study demonstrates the potential of nano-enhanced biodiesel as a viable partial replacement for conventional diesel in CI engines, with further optimization needed to mitigate NO_x emissions.

Keywords: Castor; biodiesel; Nanoparticle; Oxidation stability; performance; Emission Performance; Combustion

1. Introduction

Energy is essential for the development of nations and plays a critical role in both social and economic progress [1]. It serves as the foundation for enhancing the quality of life and enabling investments and innovations that drive various sectors. Moreover, energy is key to improving transportation networks, which are vital for trade and commerce. Efficient transportation systems rely on energy to move goods and people, helping to connect markets and stimulate economic activity. As the global population continues to grow rapidly, energy demand is increasing, leading to challenges in energy security and environmental sustainability. Additionally, the rising price of crude oil and its associated emissions have prompted a strong market push towards sustainable fuels for future generations. This global warming and other environmental considerations, in addition to scarcity of fossil fuels have triggered the search for fuels which are environmentally friendly and abundant. The non-environmentally friendly power sources are supposed to drain one day [2]. Some of non-environmentally friendly energy's derived from limited resources that will eventually run out are such fossil fuels like coal, oil, and natural gas. Furthermore, the primary disadvantages of burning fossil fuels include their emissions and pollution, as well as their exhaustibilities, non-recyclability, and difficult disposal of their byproducts [3]. In addition to being the primary cause of climate change, burning fossil fuels and biomass has a significant negative impact on human health, as air pollution is thought to be the cause of at least five million deaths annually [4]. In generally, to remove this drawback of non-renewable energy resource using renewable energy is the best option.

The transportation sector is still heavily dependent on fossil fuels, especially since internal combustion (IC) engines are made to transform heat into mechanical energy so that cars can move. In addition to highlighting the significance of fossil fuels in the current transportation infrastructure, this dependence presents difficulties in lowering greenhouse gas emissions. For sustainability and environmental preservation, the industry's need to innovate and embrace cleaner technology makes the switch from internal combustion engines to electric and alternative fuel vehicles all the more important. Conventional fuels for internal combustion engines include gasoline and diesel. Researchers and car producers are looking for alternative fuels that can either totally or partially replace conventional fuels. The cause is the energy security issue of traditional crude-based fuels, as well as increased exhaust gas emissions from IC engines powered by gasoline

and diesel fuel. This shifting of energy source in to renewable source is gradually integrating modern technologies and fuel alternatives [5]. Alternative fuels are one of the types of fuels that are extracted from various biomass sources that act as a suitable substitute for fossil fuel. This alternative fuels are reliable energy sources and they are abundant, clean, eco-friendly and can be renewed types of energy sources [6]. Generally, the world communities need alternative energy sources to reduce the negative environmental impact. Biodiesels are one of the sources of alternative fuels that partially replace fossil fuels in recent times to keep the sustainability of resources and the environment. Biodiesels are one of the liquid types of biofuels.

Research indicates that castor oil-derived biodiesel has gained recognition as a viable alternative to traditional diesel fuel. Biodiesel made from castor oil offers several environmental benefits; its successful integration into existing diesel engine systems necessitates a comprehensive understanding of its performance characteristics. It offers major advantages, including lower emissions of CO, HC, SOx, and particulate matter, along with improved lubricity and biodegradability [7],[8]. Its inherent oxygen content (10–11%) enhances combustion efficiency, reducing lifecycle CO_2 emissions by up to 78%. However, issues such as high viscosity, limited oxidation stability, and elevated NOx emissions remain significant challenges [9],[10],[11].

The current study concentrates on evaluating and comparing the impacts of single and hybrid nanoparticles on engine performance and emissions [12],[13]. Biofuels such as biodiesel, bioethanol, and biogas are renewable, biodegradable, and can be produced from various feedstocks, including oils, waste residues, algae, and animal fats [14]. Nanotechnology has recently been explored to further improve biodiesel combustion and emission characteristics. Metal oxide nanoparticles such as Al_2O_3, TiO_2, CeO_2, and ZnO enhance fuel atomization, promote oxidation, and increase heat transfer within the combustion chamber [15],[16]. These additives have been shown to reduce CO, HC, and soot emissions while improving brake thermal efficiency (BTE) and lowering specific fuel consumption (SFC). To prevent nanoparticle agglomeration, surfactants such as CTAB or SDBS are typically employed to ensure stable dispersion [17]. Experimental results demonstrate that Al_2O_3 and TiO_2 nanoparticles at 20–40 ppm concentrations can enhance BTE by up to 17.6% and reduce CO and NOx emissions by approximately 20% and 10%, respectively [18],[19],[20].

This study presents a novel investigation into the combined influence of aluminum oxide (Al_2O_3) and titanium dioxide (TiO_2) nano-additives on the performance, combustion, and emission characteristics of a compression ignition engine fueled with castor oil biodiesel blends. Unlike most previous works that employed single nanoparticles or conventional feedstocks, this research introduces a hybrid nano-additive system applied to castor biodiesel a non-edible, underutilized, and locally abundant feedstock. The synergistic catalytic effects of Al_2O_3 and TiO_2 improved fuel atomization, combustion efficiency, and emission quality, achieving a 10.3% increase in brake thermal efficiency and a 13.9% reduction in brake specific fuel consumption. These findings highlight a sustainable, innovative approach to enhancing biodiesel performance and contribute new insights into nano-catalytic fuel optimization for renewable energy applications.

2. Materials and methods

2.1 Chemicals

Solvents and chemicals, such as hexane 99%, Span 80 (Surfactant), methanol (CH3OH, 99.8 %), ethanol (C2H5OH, 99.9 %) and potassium hydroxide (KOH, 85%). Additionally, different physicochemical characteristics of the castor oil and biodiesel were also evaluated using phenolphthalein indicator, hydrochloric acid, diethyl ether, Wij's solution, sodium thiosulfate solutions, and starch solution and others were purchased from local chemical vendors.

2.2 Equipment

In this research, various equipment was utilized, including a solvent auto-extractor (VELP SCIENTIFICA, SER158) for extracting oil from castor seeds; and a magnetic stirrer for mixing during biodiesel production. Additionally, a Rancimat was used to assess the oxidation stability of the biodiesel, while an FTIR spectrometer was employed to analyze functional groups. The surface morphology was examined using SEM-EDX (COXEM, Korea), and gas chromatography (Agilent 7890) was conducted to identify the chemical composition. A surface area analyzer (Horiba SA-9600) was utilized to determine the surface area of the particles, and a bomb calorimeter was used to measure the heating value of the biodiesel.

2.3 Oil Extraction

Castor seeds were gathered from the Bale Goba Oromia in Ethiopia for this study. Following the completion of the seed collection, the seeds were sun-dried and decorated, as illustrated in Figure

1 (A), (B) and (C). Seed can be obtained by decorticating the castor capsule (fruit). Additionally, the seed's decortication yields the embryo, which contains the oil. Following a 24-hour oven drying period, the seed was cleaned, decorticated to extract the embryo, ground in a fine grinder, and then put through the oil extraction procedure. The extraction of oil from castor seeds was conducted using two distinct methodologies to compare yield under laboratory and large-scale conditions: a solvent-based Soxhlet extraction as shown in Figure 1 (D) and (E), and a hydraulic oil pressing shown in Figure 1 (F).

For the analytical-scale procedure, a Solvent AutoExtractor SER158 was utilized for Soxhlet extraction of ground, de-shelled castor seeds. A precise 7-gram sample was accurately weighed and placed within a filter paper thimble. This thimble was then subjected to a continuous extraction cycle with 100 mL of n-hexane. The process was optimized on the instrument's "Total fat in oily seeds" program, which maintained the solvent at its boiling point of approximately 70 **°C**. The n-hexane vaporized, moved upward and condensed over the biomass, dissolving the lipid components. The resulting lipid-rich solvent drained back into the flask, thereby initiating a new extraction cycle. This controlled, repeated reflux effectively maximized lipid recovery while minimizing solvent loss. The extraction was performed for a total duration of 2 hours and 35 minutes, with the condenser cooled by a consistent tap water flow of 3.3 L/min. A rotary evaporator was used to carefully remove the solvent from the oil after extraction. After that, the oil yield was calculated quantitatively using the formula shown in Equation 3.1, which expresses the mass of the recovered oil as a percentage of the initial dry sample mass. This metric served as a direct assessment of the extraction process's efficiency [21].

In parallel, large-scale oil production was performed on whole castor seeds using a hydraulic oil extraction press machine. This method was employed to measure the oil production yield directly from the pressing without the use of chemical solvents. This approach provided a practical comparison of extraction efficiency between laboratory-controlled solvent-based methods and industrial mechanical pressing. The quantity of oil that was extracted was determined by: -

$$\% \text{ Oil yield} = \frac{\text{Mass of castor oil}}{\text{Mass of castor seed powder}} \times 100 \ldots\ldots\ldots\ldots\ldots (3.1)$$

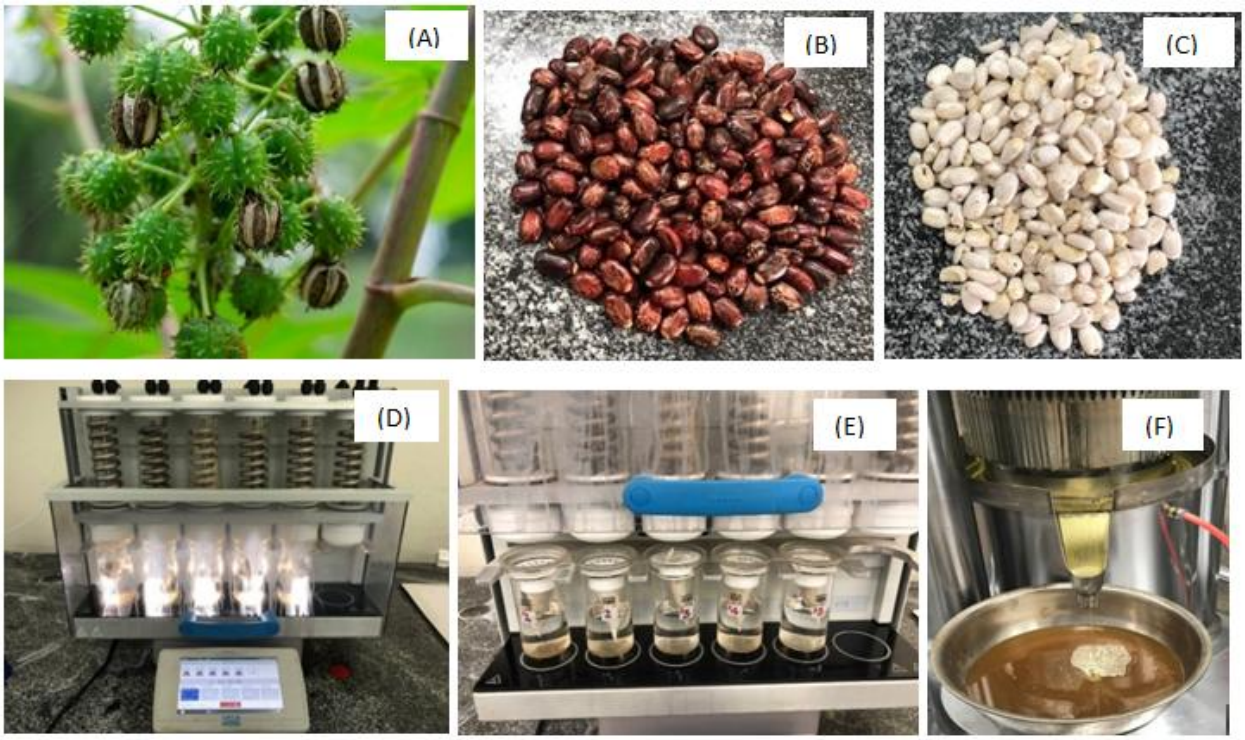


Fig. 1 Castor oil extraction (A) Castor Fruit, (B) Castor seed, (C) An embryo, (D) Using a Soxhlet extractor to extract oil, (E) Final result oil and (F) A hydraulic oil press used for mass production of castor oil extraction.

2.4 Biodiesel production

Biodiesel was synthesized from castor oil via a potassium hydroxide (KOH)-catalyzed transesterification with methanol. The procedure commenced by heating the oil to 60°C while stirring at 650 rpm as shown in Figure 2. Separately, a solution of methanol was prepared, with a mass equivalent to one-third of the initial oil weight, corresponding to an alcohol to oil molar ratio of 9:1. At a concentration of 1.25 weight percent in relation to the oil, this methanol was mixed with a KOH catalyst.

Biodiesel was synthesized from castor oil through a potassium hydroxide (KOH)-catalyzed transesterification reaction using methanol as the alcohol component. Initially, the castor oil was heated to a temperature of 60°C and maintained under continuous mechanical stirring at 650 revolutions per minute (rpm), as depicted in Figure 2. Concurrently, a methanol solution was prepared with a mass equivalent to one-third of the oil's initial weight, corresponding to an alcohol-

to-oil molar ratio of 9:1. This methanol was blended with potassium hydroxide at a concentration of 1.25 wt.% relative to the oil mass to form the catalyst-alcohol mixture.

The prepared methanol-KOH solution was then gradually introduced into the heated oil while maintaining stirring at 650 rpm. The transesterification reaction was conducted for 90 minutes at a constant temperature of 60°C to facilitate the conversion of triglycerides into methyl esters (biodiesel) and glycerol. Upon completion of the reaction, the mixture was allowed to cool naturally to ambient temperature (approximately 25°C) over an extended period of 8 hours. Following this cooling phase, the acidity of the reaction mixture was assessed, and any residual alkalinity was neutralized to a pH of 7 by the careful addition of 46% hydrochloric acid (HCl), thereby stabilizing the biodiesel product.

Subsequently, the crude biodiesel underwent a purification stage, involving multiple washings with hot distilled water, repeated ten times to effectively remove impurities such as residual methanol, catalyst residues, and glycerol. Post washing, the biodiesel was subjected to drying on a hot plate maintained at 110°C for one hour, ensuring complete evaporation of any residual methanol. The purified biodiesel was then cooled in open air for approximately 30 minutes to stabilize prior to storage or further analysis.

The glycerol phase containing the catalyst was processed to recover the potassium hydroxide catalyst, which was dried in an oven at 80°C for one hour to remove moisture and prepare it for reuse. This catalyst recycling protocol was tested for up to two cycles to evaluate its catalytic efficacy and potential degradation upon reuse.

Finally, the yield of biodiesel from each batch was quantitatively determined using the specific formula outlined in Equation 2-1, ensuring accurate assessment of process efficiency. This methodological framework not only enables the efficient synthesis and purification of high-quality biodiesel from castor oil but also integrates catalyst recovery and reuse strategies, contributing to the overall sustainability and cost-effectiveness of the biodiesel production process [22]. Then finally characterization of pure biodiesel.

$$\text{Biodiesel yield (\%)} = \frac{\text{Mass of castor oil sample}}{\text{Mass of castor oil used}} \times 100 \quad \ldots\ldots\ldots\ldots\ldots\ldots\ldots\ldots \quad (2.1)$$

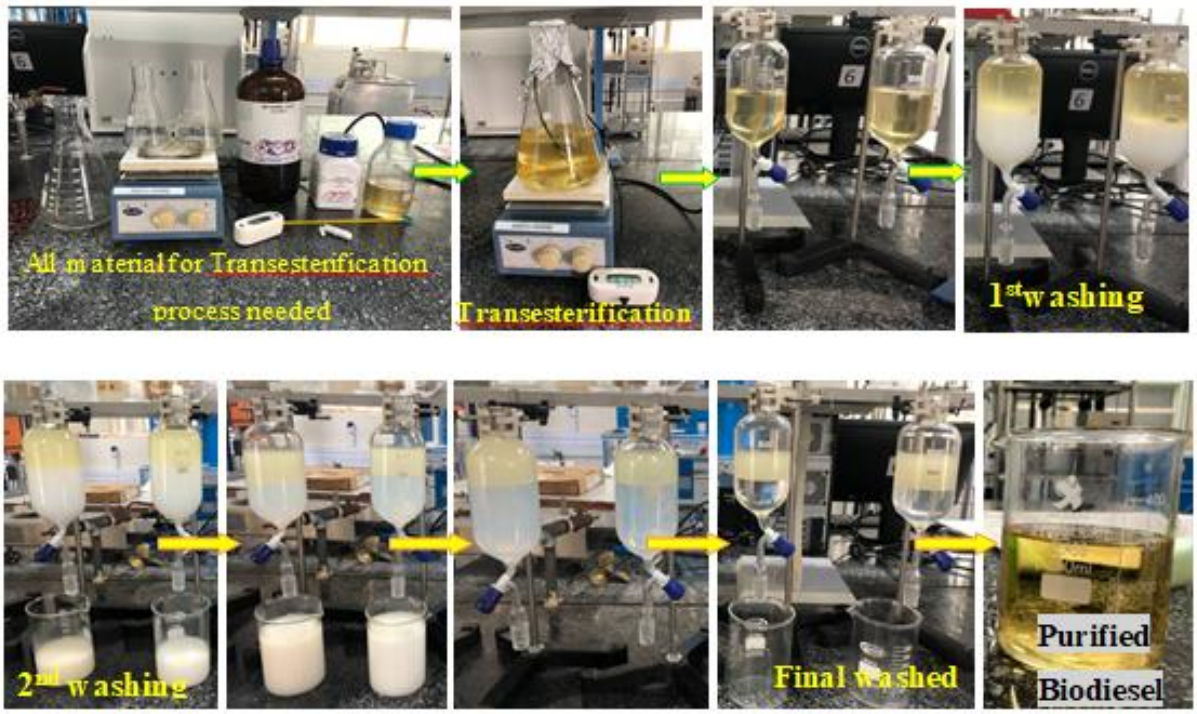


Fig. 2 General stapes in Transesterification process

2.5 Test fuel preparation

Biodiesel can be used alone or by mixing with diesel. The differing chemical compositions of biodiesel and diesel can lead to changes in physicochemical properties, which in turn impact engine performance and the levels of pollutant emissions generated. The Castor Biodiesel (B) was mixed with conventional petroleum diesel at four distinct levels: 10%, 15%, 20%, and 25 Vol% it is considered as B10, B15, B20, and, B25 respectively. The optimal B20 blending ratio for castor biodiesel was adopted, due to its widely recognized balance between environmental benefits and engine performance as established by the authors' previous studies [23]. To enhance the combustion characteristics of B20, nanoparticles were introduced in varying concentrations: 50 ppm for individual Al_2O_3 and TiO_2, and 40 ppm, 60 ppm, and 80 ppm for hybrid Al_2O_3-TiO_2 combinations. These blends were formulated as nano-emulsions using a two-step stabilization approach: ultrasonication Soni prep 150plus (MSE, UK) (typically at 25 kHz) break apart agglomerates and surfactants (Span 80 2% for each sample) for 20 minutes mixing to ensure long-term dispersion stability by preventing re-agglomeration and sedimentation [24]. The surfactants reduce interfacial tension between nanoparticles and the biodiesel medium, creating a stable colloidal system that ensures consistent nanoparticle activity during fuel injection and combustion

[25]. Following this, blends were prepared by using a mechanical stirrer (IKA EUROSTAR 60) for 1hrs and 30 min at 650 rpm to obtain a uniform mixture. Physical and chemical characteristics were then determined using ASTM standard procedures [26]. The resulting blend was allowed to stand undisturbed for a sufficient period of three weeks to assess its stability and monitor for any signs of component separation. Subsequent testing was only performed after confirming the absence of phase separation [27]. It markedly lowers emissions of pollutants such as CO, HC, CO2, NOx and particulate matter, while preserving strong engine performance and compatibility. The blend offers substantial environmental improvements without minimal need for engine modifications, making it a practical and cost-effective choice. This blend demonstrated satisfactory performance and compatibility with unmodified CI engines. The physicochemical properties of all test fuels were experimentally determined and are depicted in Table 1.

Table 1 Test fuel properties

Properties	Biodiesel – Diesel blend and Biodiesel-diesel- nanoparticle blends								
	B10	B15	B20	B25	B20A50 Ppm	B20T50 Ppm	B20A20 T20 ppm	B20A30 T30 ppm	B20A40 T40 ppm
Density (kg/ m^3 at 15ºc)	837.15	840.68	844.24	847.8	844.25	844.25	844.27	844.28	844.29
Kinematic viscosity (mm^2/s at 40 ºc)	3.9	4.03	4.09	4.12	3.83	3.83	3.85	3.77	3.75
Lower Calorific Value (MJ/Kg)	42.79	42.685	42.385	42.47	42.38	42.383	42.382	42.382	42.382

2.6 Nanoparticle characterization

Al_2O_3 and TiO_2 catalysts were examined using SEM-EDX (COXEM, Korea). Before being put into the SEM chamber, the Al_2O_3 and TiO_2 particles were covered with a thin coating of conductive substance, such as gold, to prevent them from becoming charged when exposed to the electron beam. A concentrated electron beam that interacts with the sample's atoms to produce signals allows the SEM to scan the surface of the sample and provide high-resolution pictures of the

particle's surface. They morphology and forms of the particles were examined by analysis of these pictures. Additionally, the surface of the sample emits distinctive X-rays due to the electron beam of the SEM. An EDX detector records these X-rays, which correspond to certain elements in the sample. The system then generates a spectrum that indicates the components that are present. The strength of the peaks in the spectrum is then measured to determine the relative concentrations of these elements.

The chemical makeup, purity, and potential pollutants of the two nanoparticel catalysts were also assessed using FTIR. In order to capture all possible absorbance peaks associated with NPs, After being prepared, the samples were placed in the FTIR spectrometer, which was set up to detect wave numbers between 4000-400 cm-1. When the two NPs samples are subjected to the FTIR's infrared beam, certain wavelengths that correspond to the molecular vibration are absorbed. The six bands of absorption associated with TiO_2 and Al_2O_3 are finally recognized. The particle is guaranteed to include TiO_2 and Al_2O_3. Also XRD were used determine the atomic and molecular structure of a material.

2.7 Experimental setup

As depicted in Figure 3, a GUNT model CT110 engine dynamometer test setup, incorporating a CT110.23 water-cooled, naturally aspirated diesel engine was employed to analyze the engine's experimental response. The setup utilized an asynchronous motor for engine starting and load application and was equipped with various sensors and actuators for precise measurement and control. Before the experiment, the engine was operated on pure diesel for 15 minutes to ensure stabilization. Experiments were conducted at a constant engine speed of 2700 RPM with variable engine loads ranging from 0 to 80%. Engine loading was capped at 80% because operating beyond this point led to instability. Combustion parameters were derived from pressure-crank angle diagrams and recorded via a data acquisition system connected to a flush-mounted piezoelectric pressure transducer in the cylinder head. A series of 100 consecutive cycles was measured during combustion analysis to reduce inter-cycle variation. Exhaust emissions were quantified using specific analyzers: HC by Infralyt smart (SAXON Junkalor GmbH, Dessau, Germany), and CO and NOx by a Seitron S500 exhaust gas analyzer (Seitron Americas Inc., Trevose, PA 19053 - USA). Detailed engine specifications are presented in Table 2.

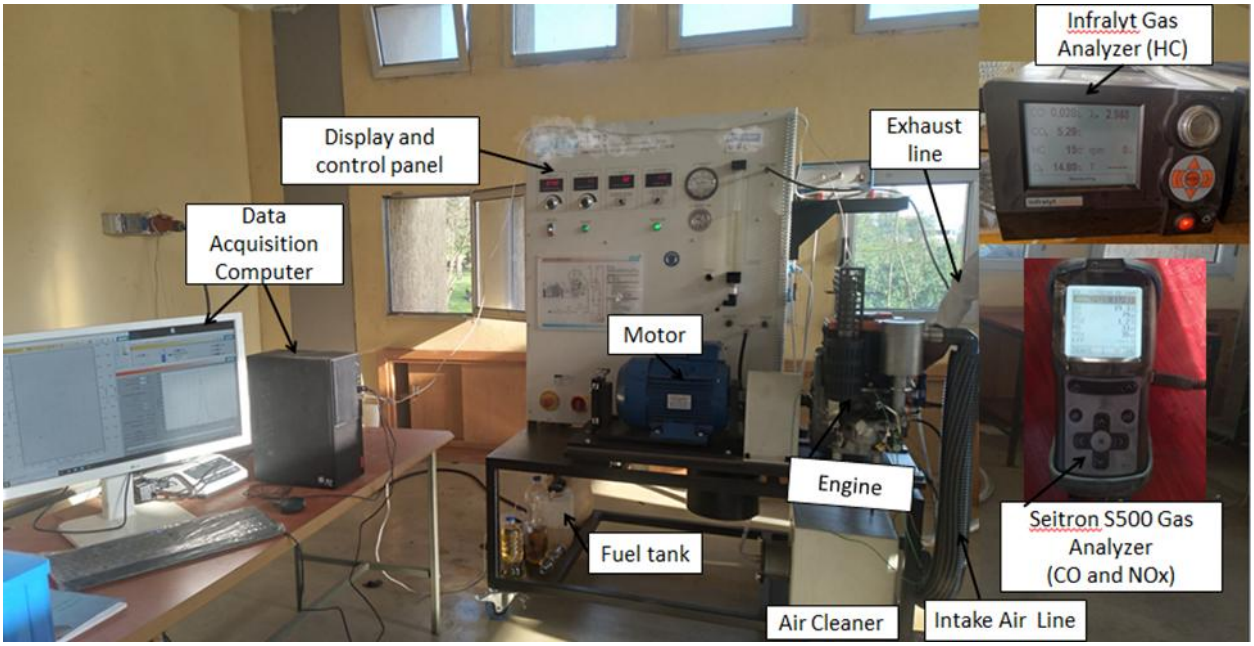


Fig. 3 Schematic arrangement of the test engine setup

Table 2 Technical specification of the engine

Brand	Kubota
Type	EA300-E2-NB1
Cylinder	Single-cylinder CI engine
Cycle	4-stroke
Injection	Direct injection
Engine type	Water-cooled
Cooling type	Diesel
Crank radius to connecting road length ratio	0.25
Swept volume (cm^3)	309
Bore x Stroke (mm)	75 x 70
Output power (kW)	5.1 at 3000 RPM
Compression ratio	23:1
Injection timing	23 ^oCA bTDC

2.8 Heat release rate (HRR) calculation

The HRR referred to here is the apparent heat release, which can be calculated based on the first law of thermodynamics without accounting for heat transfer to the cylinder wall or other losses. The HRR can be determined using Eq. 2.2 [23]. This calculation has been done by digitizing P-θ

data at a constant speed of 2700 rpm under 0%, 20%, 40%, 60%, and 80% engine load for all test fuels.

$$\frac{dQ}{d\theta} = \left(\frac{\gamma}{\gamma-1} * p * \frac{dv}{d\theta}\right) + \frac{1}{\gamma-1} * V * \frac{dp}{d\theta} \quad \text{..... (2.2)}$$

Where V is for instantaneous engine cylinder volume based on the crank angle θ, dQ/dθ is the heat release rate, p is the instantaneous pressure based on the crank angle θ, dp/dθ is the pressure rise rate, dV/dθ is the change in volume with a change in crank angle, and γ is the specific ratio adopted as 1.35.

2.9 Uncertainty analysis

The cumulative uncertainty for this system is determined using Eq. 2.3 which accounts for the propagation of uncertainties from individual measurement parameters. This calculation follows the principles of uncertainty analysis, where the total uncertainty is derived by considering the contributions of various measured variables and their respective sensitivities. Mathematically, if a dependent variable R is a function of multiple independent variables (x_1, x_2, ..., x_n), Ui the uncertainty associated with each independent parameter xi, ∂R/∂xi is the sensitivity coefficient of the function R with respect to x_n, the total uncertainty U_R of the dependent parameter such as BTE, BSFC and HRR is computed using the root sum square (RSS) method using Eq. (2.3). Consequently, the overall percentage of uncertainty was determined to be ±3.94% using Eq. (2.4) based on the respective uncertainties for each parameter detailed in Table 3.

$$U_R = \sqrt{\left[\left(\frac{\partial R}{\partial x_1}U_1\right)^2 + \left(\frac{\partial R}{\partial x_2}U_2\right)^2 + \cdots + \left(\frac{\partial R}{\partial x_n}U_n\right)^2\right]} \quad \text{..... (2.3)}$$

$$\text{Overall Uncertainity} = \sqrt{\begin{bmatrix} (\text{Speed})^2 + (\text{Brake Torque})^2 + (\dot{m}_f)^2 + \\ (\text{CP})^2 + (\text{BP})^2 + (\text{EGT})^2 + (\text{HC})^2 + \\ (\text{NOx})^2 + (\text{CO})^2 + (\text{BTE})^2 + (\text{BSFC})^2 + (\text{HRR})^2 \end{bmatrix}} \quad \text{..... (2.4)}$$

$$= \sqrt{\begin{bmatrix} (0.11)^2 + (1.39)^2 + (1.63)^2 + (0.79)^2 + \\ (0.15)^2 + (2.05)^2 + (1.67)^2 + \\ (1.21)^2 + (0.58)^2 + (0.78)^2 + (0.79)^2 + (0.52)^2 \end{bmatrix}}$$

$$= \pm 3.94\%$$

Table 3 Summary of instrument, measurement ranges, and associated percentage uncertainties

Instrument	Measured parameters	Range	Uncertainty
Tachometer	Speed	0–3000 rpm	±0.11%
Load cell	Brake torque	0-14 Nm	±1.39%
Flowmeter	$\dot{m}_f$	0-150 cm3	±1.63%
Pressure transducer CT 100.13	CP	0-250 bar	±0.79%
Thermocouples	EGT	0–1300 K	±2.05%
Infralyt smart analyzer	HC	0-2500 ppm	±1.67%
Seitron S500 analyzer	CO	0-4000 ppm	±0.58%
Seitron S500 analyzer	Nox	0-2000 ppm	±1.21%
Uncertainty in computed parameters			
Brake power (BP)	Using engine torque and speed	-	±0.15%
BSFC	Using brake power and fuel flow rate	-	±0.79%
BTE	Using brake power and lower heating value	-	±0.78%
HRR	Using CP, V, and CA	-	±0.52%

3 Results and discussion

3.1 Biodiesel production

Seed collection was performed from the castor tree manually using manpower. The amount of usable seed extracted from the dried fruit was measured. It was found that from 1 kg of sun-dried fruit, approximately 46.0% (or 460 grams) constitutes effective seed suitable for oil extraction. Consequently, to obtain 1 kg of effective seed, about 5 kg of castor fruit is needed. After seed preparation, oil extraction was carried out using a chemical method. The Soxhlet extractor yielded an oil extraction rate of 55.098%. This oil yield percentage closely aligns with previously reported

values [28], [29] from castor seed, yet higher than the oil yield reported from Croton Macrostachyus seed (CMS) by [26].

Next to extraction the transesterifation and degumming processes that was mention in chapter 3 are done respectively. The catalyst potassium hydroxide (KOH) at a concentration of 1.25% w/v and methanol were mixed in a 9:1 methanol to castor oil ratio to form a proper solution known as methyl ester oils. This mixture was stirred using a magnetic stirrer at an optimal temperature of approximately 60°C for 90 minutes [28]. After transesterification, the mixture was cooled, transferred to a separating funnel, and left for 24 hours, resulting in two layers: glycerol (bottom) and biodiesel (top). The glycerol was drained off, and the biodiesel underwent purification by washing twice with 50% heated distilled water at 80 °C to remove residual catalyst and methanol. This washing process was repeated until the water layer became clear, yielding 1000 ml of castor biodiesel with a 94% yield.

Then Blending process is proceeding. Biodiesel produced from n-pentanol and castor oil was mixed with petroleum diesel. The blends were prepared in a beaker using an electric stirrer and a glass flask at room temperature for 15 minutes. Three different blend ratios were created: B0, B100, B10, B15, B20, B25 and added nanoparticle (B20A50, B20T50, B20A20T20, B20A30T30, B20A40T40) in B20 in different concentration starting from 20ppm to 50ppm. To mix the nano particle well with the biodiesel and fuel used water base ultrasonic for 15 minite. Each mixture was stirred with a magnetic stirrer at 650 rpm for 30 minutes. Then all blends are ready for test and characterization as shown in Figure 4.



Fig. 4 Biodiesel and Diesel blend with nanoparticles

3.2 Biodiesel characterization

The key physicochemical properties of castor oil and its biodiesel such as density, specific gravity, viscosity, acid value, heating value, flash point, iodine value, moisture content, saponification value, and cetane number were measured according to ASTM standards (see Tables 4 and 5). These values were then compared with the specifications set by ASTM D6751 and EN 14214 biodiesel standards. The results confirmed that all measured properties of castor biodiesel meet the required criteria, validating its suitability for use in internal combustion engines.

Table 4 Characteristics of crude and refined castor oil

Properties	Crude castor oil	Refine castor oil
Density at 40^0C (kg/m^3)	894.787	885.363
Specific gravity at 15^0C	0.950	0.94
Moisture content (%)	0.378	0.218
Kinematic viscosity at 40°C (mm^2/s)	317.2	285
Saponification ()	184	182
Acidic Value	3.29	2.33
Free Fati Acid	1.645	1.165
Iodine Value	82	82.5

Table 5 The overall physicochemical property of the castor biodiesel and compared with CMS.

Properties	Present study	Castor [28]	Castor [29]	CMS [26]	Biodiesel standard	
					ASTM D6751	EN 4214
Density at 15^0C (kg/m^3)	901.2	900	922	846.30	820-900	860-900
Kinematic viscosity at 40°C (mm^2/s)	17	14.7	17.4	4.4	1.9-6.0	3.5-5.0
Lower Calorific Value (MJ/Kg)	40.4	41.0	39.5	40.4	Min 38.00	Min 35.00
Cloud point °C	-15	-14	-12	-9	-15 to 5	-3 to 12

Pour point ºC	-28	-26	-26	-15	-35 to -15	-15 to 16
Flash point	210	198	215	175	Min 100-170	Min 120
Fire point	220	217	220.5	210	-	-
Saponification	181.26	186.6	184	192.77	≤ 215.99	≤ 218.79
Acidic Value	0.28	0.36	-	0.22	Min 0.80	Min 0.50
Free Fati Acid	0.14	0.18	-	0.11	≤ 0.4	≤ 0.25
Iodine Value	83.5	89	-	105.45	-	120
Cetan number	57.66	-	-	50.89	Min 47	Min 51
Oxidation stability (h)	16.14	-	-	2.39	-	-
Oil yield %	94	93	92	96	-	-

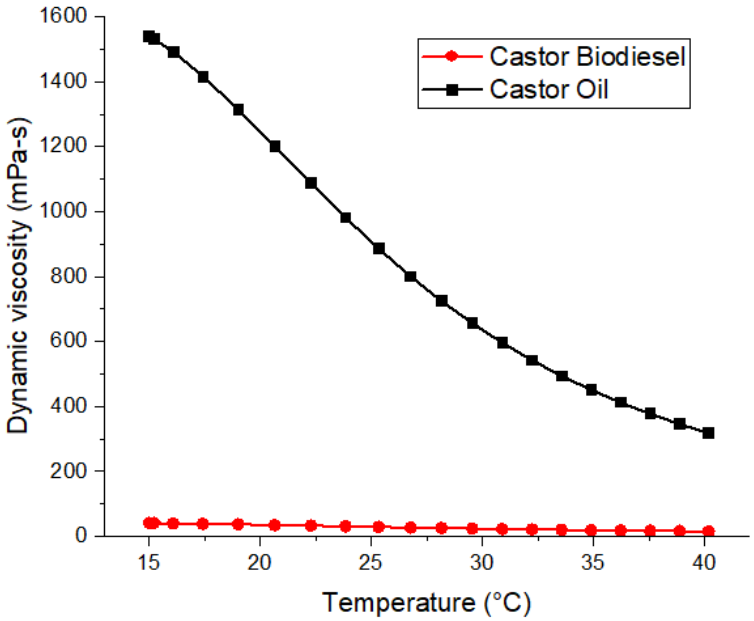


Fig. 5 Dynamic viscosity of castor oil and biodiesel

A rheometer was used to measure viscosity of the oils at 40°C. The raw castor oil had a dynamic viscosity of 317 mpa s, which was reduced to 285 mpa s after refining. This viscosity was further dramatically lowered to 14.75 mpa s in the final biodiesel product. This reduction is attributed to the removal of glycerol during the transesterification process and is within the standard range for biodiesel as shown above in Figure 5.

As illustrated in Figure 6, the primary functional groups present in castor seed oil were identified using Fourier Transform Infrared (FTIR) spectroscopy. The FTIR spectrum was recorded at room temperature over a wavenumber range of 4000–400 cm^{-1}. A broad absorption band between 3500–3000 cm^{-1}, corresponding to hydroxyl (–OH) groups, suggests potential enhancements in the combustion kinetics of castor biodiesel. Prominent peaks observed at 2924.25 cm^{-1} and 2854.40 cm^{-1} are indicative of methyl ($–CH_3$) group vibrations, while the absorption at 1738.85 cm^{-1} is attributed to the stretching vibrations of carbonyl (C=O) groups typically found in carboxylic acids (–COOH), ketones (–CO–), or aldehydes (–CHO).

The peak at 1438.85 cm^{-1} corresponds to –C–H stretching in ester functionalities, while the band at 1359.96 cm^{-1} reflects the bending vibrations of $–CH_2$ groups, characteristic of compounds such as 2,4-dimethylpentane. Additionally, the absorption at 1171.29 cm^{-1} is associated with the stretching vibrations of C–O and C–O–C bonds, as well as $O–CH_3$ groups, present in both castor oil and its biodiesel derivative. The absorption band at 723.36 cm^{-1} indicates the presence of methylene ($–CH_2–$) groups, linked to their rocking vibrations in the raw oil and biodiesel samples.

Comparable FTIR results have been documented in previous studies [30]. Notably, a shift in absorption peaks from 1459.21, 1238.96, 1162.96, and 723.00 cm^{-1} in raw castor oil to 1438.5, 1359.96, 1171.29, and 723.36 cm^{-1} in castor biodiesel was observed. The disappearance of the 1238.96 cm^{-1} peak in the biodiesel spectrum, alongside the appearance of a new band at 1359.96 cm^{-1}, confirms the successful transesterification of castor oil into fatty acid methyl esters (FAMEs).

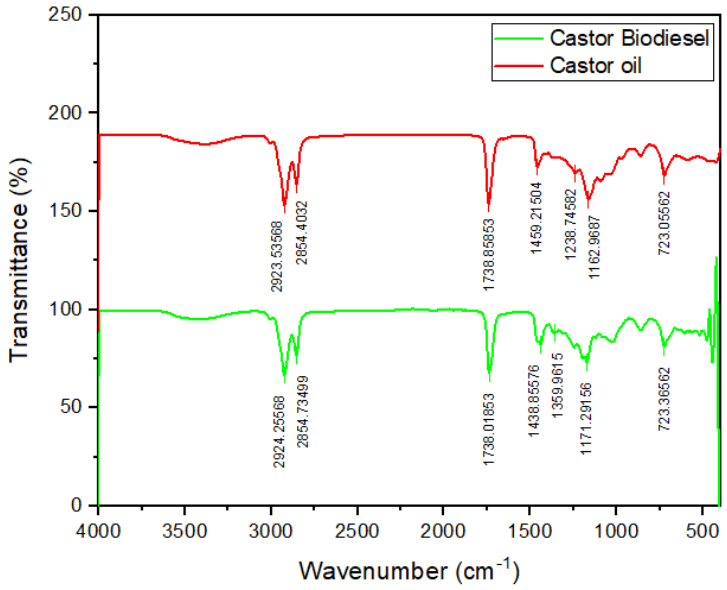


Fig. 6 FT-IR result of castor oil and biodiesel

Gas Chromatography–Mass Spectrometry (GC–MS) analysis was conducted to determine the fatty acid methyl ester (FAME) composition of castor biodiesel, which is a key factor in evaluating its physicochemical properties and fuel performance. The analysis identified three categories of fatty acids within the biodiesel: saturated (Cn:0), monounsaturated (Cn:1), and polyunsaturated (Cn:2,3), all of which influence combustion behavior, oxidative stability, and cold flow properties. As presented in Figure 7 and Table 6, the major constituent of the castor methyl ester was ricinoleic acid, accounting for 88.06% of the total FAME content. Other significant components included linoleic acid (5.07%), oleic acid (3.59%), stearic acid (1.59%), palmitic acid (1.04%), gondoic acid (0.23%), and linolenic acid (0.41%).

The overall composition of saturated fatty acids was found to be 2.63%, while unsaturated fatty acids constituted 97.35% of the total. These values, along with the detailed peak area percentages for each FAME compound, are summarized in Table 6. The dominance of unsaturated fatty acids in the castor biodiesel aligns with common trends in vegetable oil-based feedstocks, further supporting its viability for biodiesel production due to improved cold flow properties and combustion efficiency [31]. Overall, castor biodiesel is rich in polyunsaturated fatty acids, which have significantly lower melting points compared to monounsaturated and saturated fatty acids. This characteristic endows castor biodiesel with notably better cold-weather properties than many

other biodiesels. The GC–MS result obtained from castor seed biodiesel in this research is equivalent with the result reported by [32].

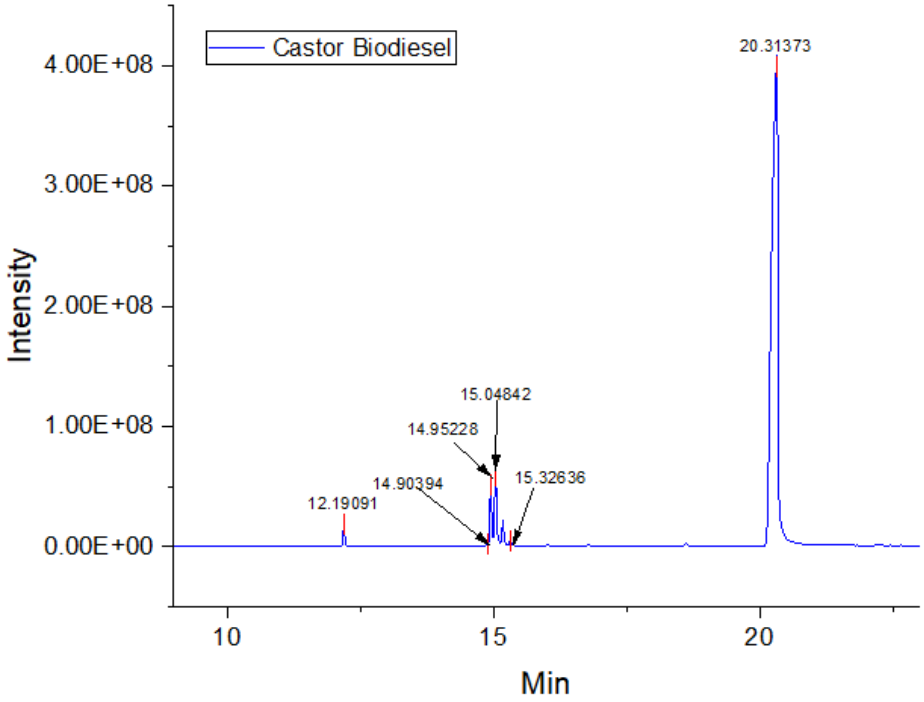


Fig. 7. GC-MS result of castor oil

Table 6 GC-MS result of castor biodiesel

Peak No.	Retention time	Area (%)	Systematic Name	Fatty acid name	Structure
1	12.1985	1.043	Hexadecanoic acid, methyl ester	Palmitic	C16.0
2	14.954	3.5892	9-Octadecenoic acid (Z)-, methyl ester	Oleci acid	C18:01
3	15.0432	5.0709	9,12-Octadecadienoic acid (Z,Z)-, methyl ester	Linoleic acid	C18:02
4	15.1809	1.5877	Methyl stearate	Stearic acid	C18:0
5	15.3225	0.4118	9,12,15-Octadecatrienoic acid, methyl ester, (Z,Z,Z)-	Alpha-linolenic acid	C18:3
6	18.607	0.2344	cis-11-Eicosenoic acid, methyl ester	Gondoic acid	C20.1
7	20.3189	88.0629	9-Octadecenoic acid, 12-hydroxy-, methyl ester, [R-(Z)]-	Ricinoleic acid.	C18:3

Saturated fatty acid (2.62%)
Monounsaturated fatty acid (3.81%)
Polyunsaturated fatty acid (93.54%)

In the present study, the oxidative stability of pure castor biodiesel was quantified via its induction period, measured to be 16.14 hours as shown in Figure 8. This induction time reflects the duration during which the fuel resists oxidative degradation under accelerated aging conditions, typically assessed using standardized methods such as EN 14112 (Rancimat method). The observed value indicates a relatively high degree of oxidative resistance, signifying that castor biodiesel possesses favorable stability characteristics, even in the absence of antioxidant additives. This prolonged induction time underscores the biodiesel's potential for long-term storage and practical applicability in fuel systems where oxidative degradation is a concern.

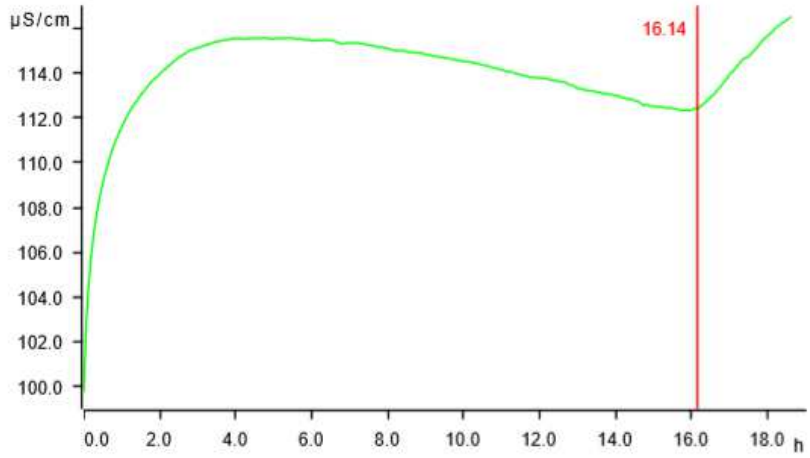


Fig. 8 Oxidation stability castor oil.

3.3 Nanoparticles characterization

The provided data compares the properties of three nanoparticles: Aluminum Oxide (Al_2O_3), and Titanium Dioxide (TiO_2). While they all have similar average particle sizes in the nanometer range, their other characteristics vary significantly. In contrast, Al_2O_3 has the highest thermal conductivity, making it better for improving heat transfer. The zeta potentials indicate all three nanoparticles have good colloidal stability, but with different surface charges. These distinct properties make each nanoparticle suitable for different applications. Generally, the nanoparticle's parameters are described in Table 7.

Table 7 Nano particle parameters

Parameters	Nanoparticles	
	Al_2O_3	TiO_2
Average Particle Size (nm)	30-50	30–40
Specific Surface area (m^2/g)	15-35	77
Zeta Potential (mV)	26.8	38.5
Thermal Conductivity (W/m·K)	40	8.4
Specific Heat Capacity (J/kg·K)	773	697
True Density (g/cm^3)	3.7	4.23
Appearance	White	White

3.3.1 FTIR analysis of Al_2O_3 and TiO_2

The FTIR spectra of aluminum oxide nanoparticles, as presented in Figure 9 (4000-400 cm^{-1}), were analyzed to identify characteristic functional groups and structural components. The spectral data exhibited two prominent bands attributable to nitrate within the functional group region. A strong absorption band at 3653.23 cm^{-1} was observed, indicative of the stretching vibrations in Al–OH bonds. A band observed at 974.20 cm^{-1} signified the presence of physiosorbed water molecules, corresponding to the H–O–H bending vibration. Structural confirmation was also provided by absorption peaks at 714.85 cm^{-1} and 444.725 cm^{-1}, representing the bending vibration of Al–O–Al and the stretching vibration of Al–O bonds, respectively. These findings confirm the existence of the boehmite (AlOOH) phase, aligning with previously reported results [30].

Also, TiO_2 was characterized by several key absorption bands as presented in Figure 10 (4000-400cm^{-1}). A broad peak at 3207.81 cm^{-1} corresponds Corresponding to the O–H stretching vibrations of surface hydroxyl groups, a prominent peak at 1635.85 cm^{-1} is attributed to the H–O–H bending vibration of physiosorbed water. A minor band at 1444.38 cm^{-1} may indicate C-H bending from organic impurities or carbonate species. The definitive signature of the titanium dioxide structure is present in the strong, overlapping peaks at 445.58 cm^{-1} and 430.27 cm^{-1}, which are attributed to the Ti-O stretching vibrations within the crystal lattice as consistent results were reported [33].

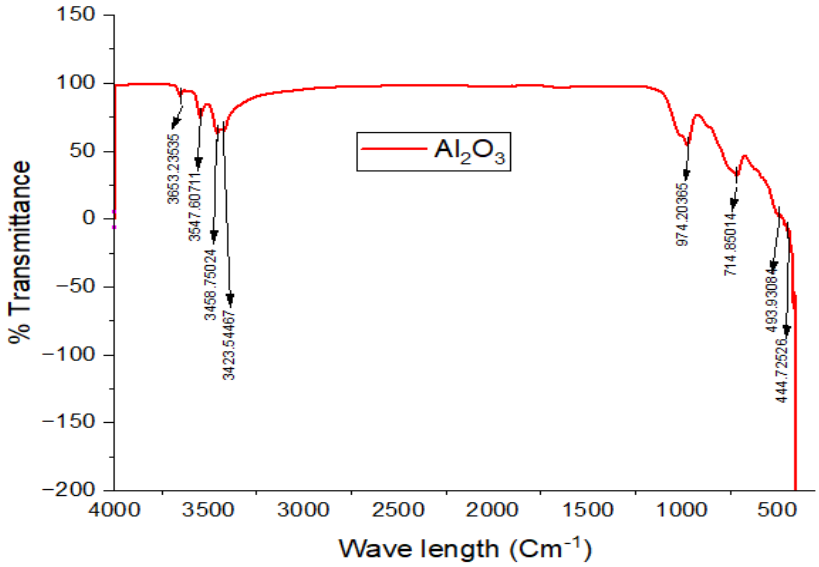


Fig. 9 FTIR Analysis of Al_2O_3 catalyst

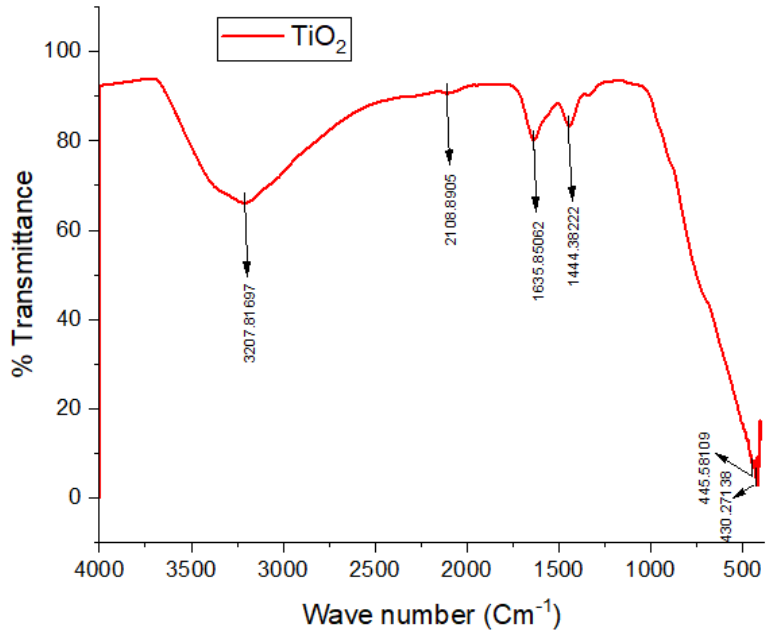


Fig. 10 FTIR Analysis of TiO_2 catalyst

3.3.2 SEM-EDX analysis Al_2O_3 and TiO_2

Characterization using SEM-EDX aims to determine morphology, particle size, and material composition. The characterization results of SEM-EDX of TiO_2 anodizing results can be observed in Figure 11. The morphology of TiO_2 anodizing results indicates the presence of 10 µm particles

(Figure 11 (a)), which are fairly evenly on all surfaces indicating the dispersed TiO_2 particles on the Ti plate surface. SEM-EDX also generates additional data in the form of X-ray energy graph. The peak position of an element in EDX depends on the energy of the element. The element will be detected at its typical energy point with intensity value on Y axis. Y-axis shows quantity values of elements in the whole sample which is later confirmed in wt%. Based on Figure 11 (b) the TiO_2/Ti anodizing results has the composition of O (oxygen) element of 22.34 wt% or 46.27 at% and Ti (titanium) element of 77.66 wt% or 53.73 at%.

Scanning Electron Microscopy (SEM) analysis was conducted to examine the morphological and structural characteristics of the synthesized catalyst, as shown in Figure 12, SEM micrographs provide crucial insights into the catalyst's surface topography, revealing a porous and fissured structure. These surface imperfections contribute to increased roughness and offer potential insights into the catalyst's physical composition, which can significantly influence the accessibility of its active sites to reactant species.

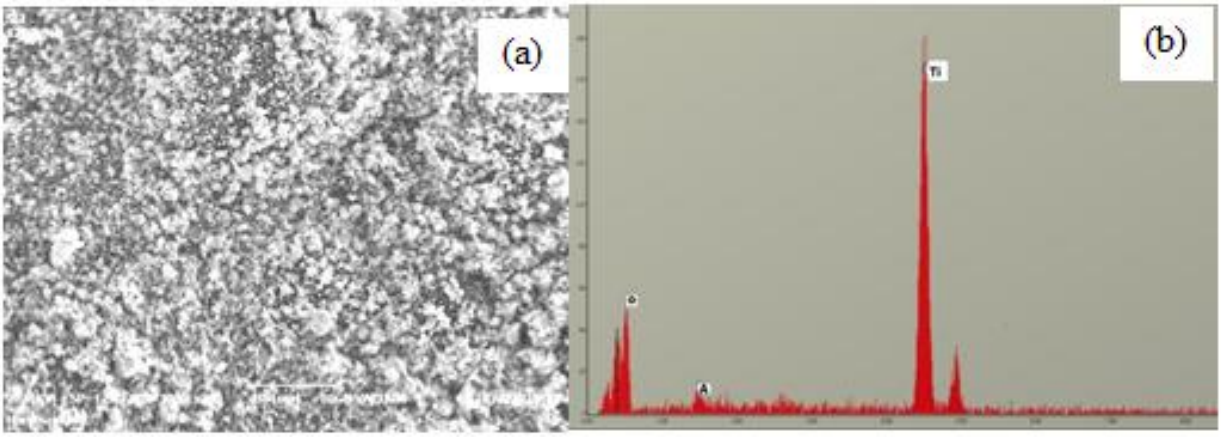


Fig 11 SEM-EDX characterization of the TiO_2 catalyst: (a) SEM images; (b) EDX spectrum analysis.

Furthermore, SEM played a key role in determining the particle size nanoparticles. The analysis determined the average particle diameter to be 1.103 μm and the average area to be 0.054 μm². This small particle size and a large specific surface area are favorable since they are directly correlated with an increased number of accessible active sites. This morphological characteristic is expected to enhance the reaction kinetics and mitigate mass transfer limitations, thereby improving overall catalytic performance.

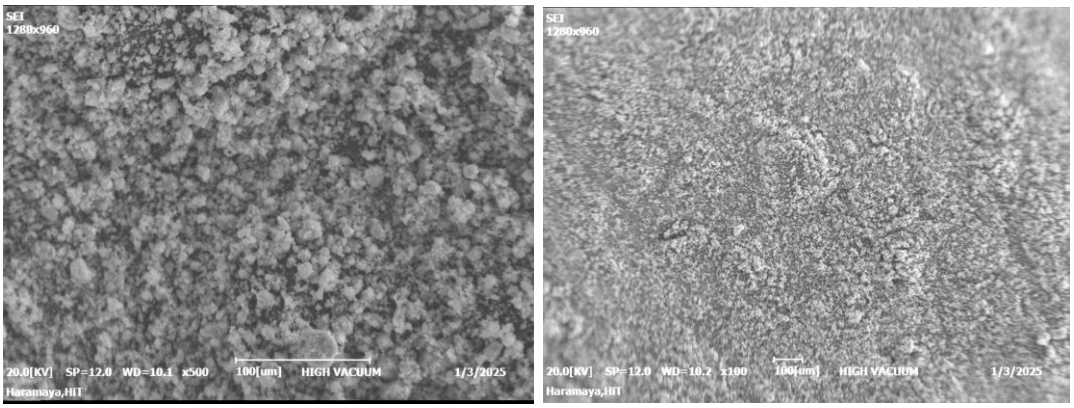


Fig. 12 SEM-EDX analysis of Al_2O_3 catalyst SEM Selected Area for Analysis (respectively)

3.3.3 XRD analysis of Al_2O_3 and TiO_2

The XRD pattern of the Al_2O_3 sample confirms its crystalline nature through sharp, high-intensity peaks. This unique diffraction fingerprint, with major peaks at 2θ values of 18.91∘, 20.46∘, and 40.74∘ as shown in Figure 13, is used to identify the specific crystalline phase, such as gamma-alumina ($\gamma-Al_2O_3$) which corresponds to the [34]. This phase identification is a critical step, as the crystal structure directly dictates the material's physical and chemical properties.

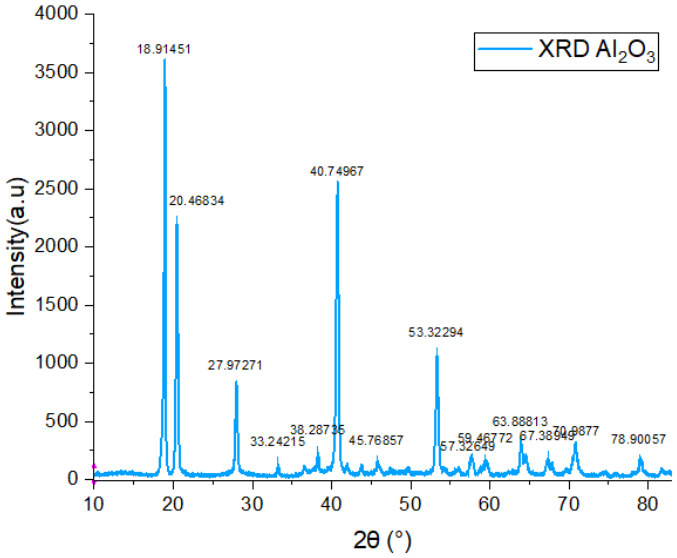


Fig. 13 XRD for Al_2O_3 Particles

According to the in-depth analysis conducted, XRD pattern of the TiO_2 sample confirms its crystalline nature as shown in Figure 14, with the broad diffraction peaks serving as a direct indication of a nanocrystalline structure, a finding supported conceptually by the Scherrer equation. The phase identification is definitively anatase, evidenced by the most intense peak located at 2θ=25.49∘, which corresponds to the [34] crystal plane. This identification is further supported by additional peaks at 38.26∘, 47.93∘, and 54.59∘. The structural information derived from this analysis is critical because the anatase phase is highly valued for its excellent photocatalytic activity.

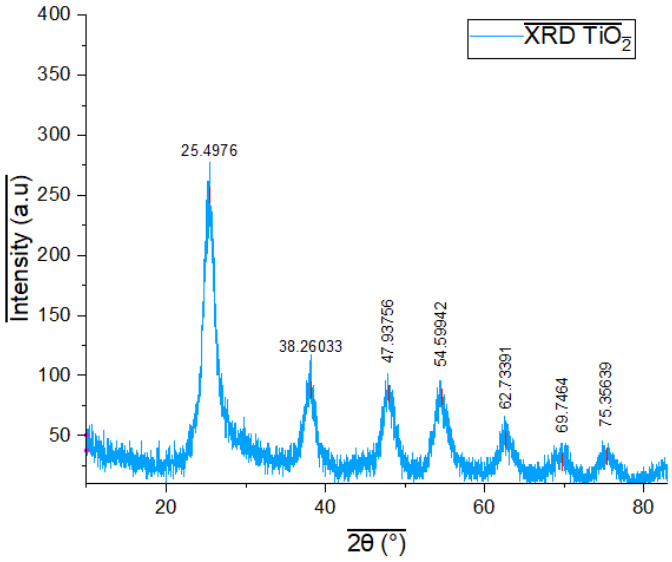


Fig. 14 XRD for TiO_2 Particles

3.4 Combustion characteristics

This study investigated castor biodiesel/diesel at different blending ratio and the impact of incorporating Al2O3 and TiO2 nanoparticles into a castor biodiesel/diesel blend (B20). Experiments were conducted in a compression ignition (CI) engine operating at a constant speed of 2700 RPM under variable loads ranging from 0% to 80%, incremented in 20% steps. The analysis encompassed a comparative evaluation of key engine performance parameters, namely brake thermal efficiency (BTE), brake specific fuel consumption (BSFC), and exhaust gas temperature (EGT), contrasting blends with and without nanoparticle additives. Furthermore, emission characteristics, specifically carbon monoxide (CO), nitrogen oxides (NOx), and unburned hydrocarbons (HC), were assessed relative to the baseline B20 fuel. The investigation

also characterized combustion attributes, including cylinder pressure (CP), heat release rate (HRR), ignition delay (ID), and the start of combustion (SoC), comparing them against the baseline B20 operation. Data reliability was ensured by replicating each test condition three times.

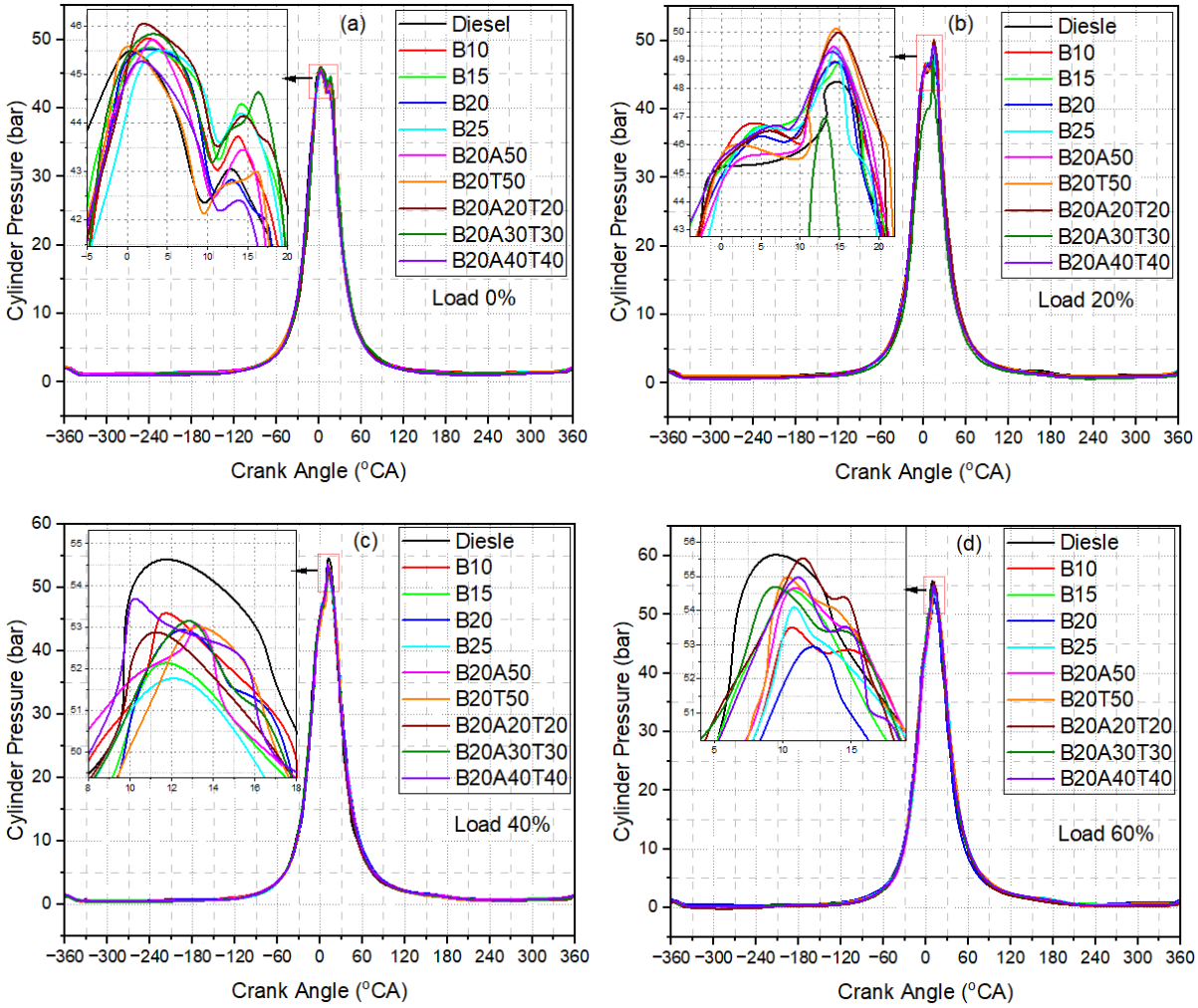
3.5 Cylinder pressure (CP)

Cylinder pressure (CP) represents the peak force generated within the combustion chamber and is significantly influenced by the rate and intensity of the combustion process. Figure 15 (a–e) illustrates the variation of cylinder pressure with crank angle at a constant engine speed of 2700 rpm, under varying load conditions of 0%, 20%, 40%, 60%, and 80%. In all load cases, pure diesel consistently exhibited lower peak CP values compared to the biodiesel blends. A clear trend was observed wherein increasing engine load resulted in higher peak cylinder pressures, primarily due to greater fuel injection required to meet elevated power demands. The rise in CP is directly linked to the exothermic nature of the combustion process, driven by fuel oxidation.

At low engine loads (0–20%), the biodiesel blends produced higher peak cylinder pressures than pure diesel. However, under higher load conditions (above 40%), pure diesel showed greater peak CP values relative to the biodiesel blends. This shift is attributed to the higher viscosity of biodiesel, which affects atomization and combustion characteristics, as previously reported in [35]. At lower engine loads where fuel injection volumes and in-cylinder temperatures are relatively low, it improved combustion characteristics of biodiesel blends contribute to higher cylinder pressures. However, as the proportion of biodiesel in the blend increases, a decline in cylinder pressure is observed, primarily due to the reduced calorific value of biodiesel, as reported in previous studies [36]. Moreover, at elevated engine loads, the higher fuel injection rates markedly influence the ignition behavior of biodiesel blends. As the biodiesel blend ratio increases up to B25, a gradual reduction in peak cylinder pressure is observed.

The incorporation of Al_2O_3 and TiO_2 nanoparticles into the B20 base fuel resulted in average increases in cylinder pressure of 1.2% and 1.5%, respectively. This enhancement is attributed to the superior thermal conductivity and increased surface area of the nanoparticles, which facilitate improved heat transfer between the fuel and particles, thereby promoting better atomization and more efficient combustion of the fuel blend. Among the fuel samples, B20A20T20 exhibited a 2.3% increase in pressure which indicates that the combination of different nanoparticles has a higher catalytic effect compared to the individual nanoparticle. The highest cylinder pressure at

B20A20T20 might be attributed to combined effect of a relatively the large surface area of TiO_2 and Al_2O_3 thermal conductivity. Additionally, the premixed combustion phase further optimizes heat transfer, resulting in a higher peak pressure due to nanoparticle interactions [37]. Similar trends in CP have been observed in studies incorporating biodiesel and nanoparticles [38].



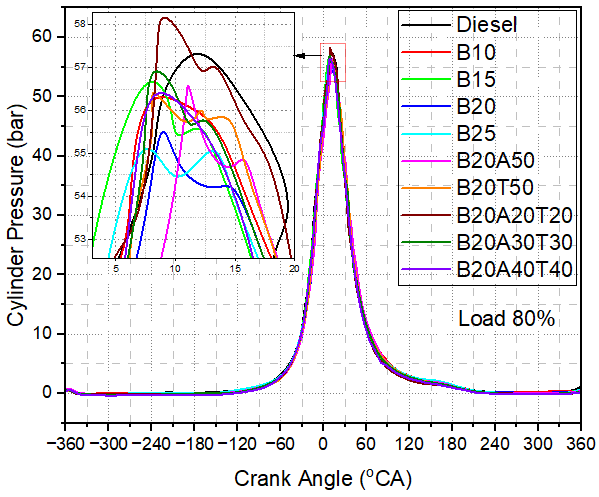


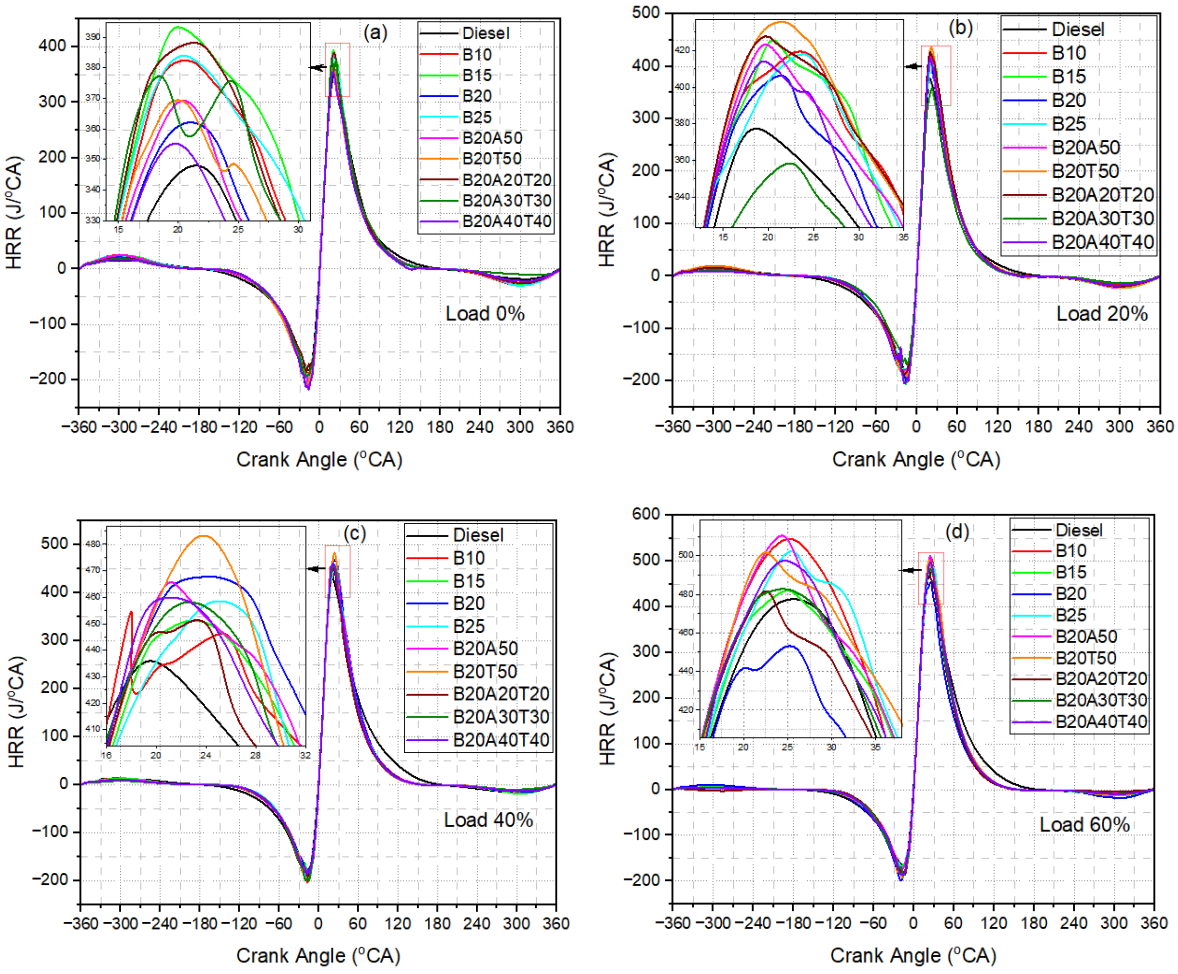
Fig. 15 Cylinder pressure of all load and samples

3.6 Heat release rate

The apparent HRR refers to the rate at which thermal energy is liberated during the combustion process, without accounting for simultaneous heat transfer losses. Key factors influencing HRR include fuel ignition quality, kinematic viscosity, and energy content, as these parameters directly affect the combustion characteristics and efficiency. The results show that heat release rate (HRR) rises with increasing engine load. At lower loads (0–40%), biodiesel blends demonstrated a 5–13% higher HRR compared to pure diesel. However, at higher loads (60% and 80%), the HRR of biodiesel blends was 5–11% lower than that of pure diesel. This decrease is attributed to the higher density and viscosity of castor biodiesel, which affects combustion as fuel quantity increases with load, as illustrated in Figure 16 (a–e). The maximum HRR recorded was 539.7 J/oCA for pure diesel, followed by 533.7 J/oCA for B10, 529.9 J/oCA for B20, 513.12 J/oCA for B25, and 479.1 J/oCA for B15. A slight decline in HRR with rising biodiesel content at high loads is observed, likely due to the richer fuel mixture increasing viscosity, which reduces volatility and HRR. Additionally, the reduction in HRR at higher loads is linked to shorter ignition delay (ID), limiting fuel–air mixing prior to ignition [39].

The influence of metalic nanoparticles (Al_2O_3 and TiO_2) was also evaluated compared to the base fuel of B20. The results indicate that incorporating nanoparticles into the B20 blend elevated the heat release rate (HRR) to levels exceeding those of pure diesel. The highest HRR of 549.4 J/°CA was for B20T50 followed by B20A50 of 540.1J/°CA compared to 529.9 J/°CA for B20. The TiO_2 increased the HRR by average 5% which is attributed to its high specific surface area, compared

to 3.8% increment for Al_2O_3. Furthermore, among the combinations of Al_2O_3 and TiO_2, B20A20T20 have shown an increased HRR by an average of 2.2% compared to B20 followed by B20A30T30 and B20A40T40. Metallic nanoparticles increased the HRR resulting from their higher thermal conductivity and improved ignitability, leading to advanced combustion onset and increased thermal energy liberation during combustion. Nanoparticles can also influence the balance between premixed and diffusion combustion.



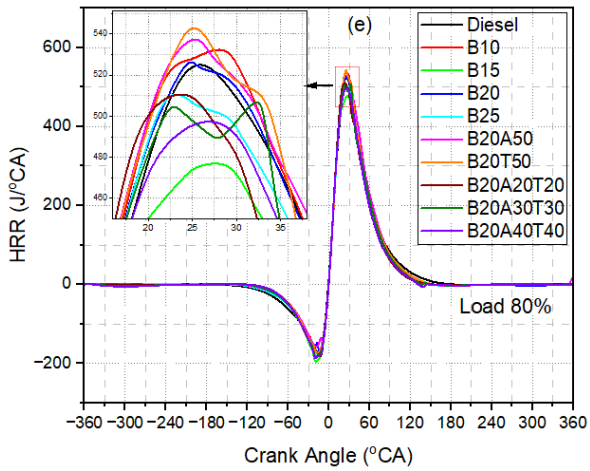


Fig. 16 Heat release rate of all samples in all loads

3.7 Engine performance characteristics

3.7.1 Brake thermal Efficiency

Figure 17 (a) presents the brake thermal efficiency (BTE) of each fuel blend across varying engine loads. BTE serves as a key indicator of how effectively fuel energy is converted into mechanical work. This study evaluated the effects of engine load and castor biodiesel blending ratios, along with metallic oxide nanoparticle additives, on BTE. The findings show that BTE increases with engine load but decreases as the biodiesel proportion rises, with the most significant drop observed at maximum load. Pure diesel achieved the highest BTE of 32.55%, while biodiesel blends showed a reduction of 6-10%. This decrease is attributed to the lower heating value, higher density, and increased viscosity of castor biodiesel blends (B10, B15, B20, and B25) compared to diesel. At maximum load, the BTE decline is likely due to the larger fuel volume in the cylinder, causing incomplete combustion. Overall, pure diesel exhibited the highest BTE under all load conditions, whereas B25 showed the lowest efficiency, mainly because of biodiesel's reduced calorific value and greater viscosity [40]. Overall, B10 demonstrated efficiency closest to that of pure diesel compared to the other biodiesel blends. The highest efficiency of 32.55% was achieved by diesel fuel at 60% load, while the biodiesel blends B10, B15, B20, and B25 showed reductions of 5.6%, 6.6%, 7.3%, and 7.15%, respectively, relative to pure diesel. A similar trend has been reported by [41]

However, the addition of both TiO_2 and Al_2O_3 nanoparticles demonstrated superior performance which resulting in a 3.3% and 4.9% % increase in BTE at 60% load, respectively. Furthermore,

the combination of Al_2O_3 and TiO_2 which is B20A20T20 enhanced BTE by 4.5% at 20% load, 10.3% at 40% load and 2.4% at 80% load, compared to B20. A further increase in nanoparticle concentration resulted in reduced in BTE by up to 8% for B20A30B30 and B20A40B40. The enhanced BTE observed with Al_2O_3 and TiO_2 is attributed to their superior heat transfer properties which improve combustion characteristics. The inherent reactivity of nano additives, along with the additional oxygen provided by partially oxygenated nanoparticles [37], also contributes to increased BTE. This aligns with the well-established positive impact of improved heat transfer rates and thermal conductivity on engine thermal efficiency [42]. At 60% load, Al_2O_3 additive exhibited higher BTE compared to TiO_2 and nanobichar. This improvement can be attributed to enhanced combustion characteristics facilitated by the relatively higher thermal conductivity and catalytic activity of Al_2O_3, which improves the cylinder combustion process.

3.7.2 Brake specific fuel consumptions

Figure 17 (b) depicts the variation of brake specific fuel consumption (BSFC) with engine load for all tested diesel-biodiesel blends. Generally, BSFC decreases as engine load increases, due to higher in-cylinder temperatures that improve fuel atomization and combustion efficiency. However, at very high loads, a slight rise in BSFC is observed, caused by incomplete combustion of an excessively rich air–fuel mixture, resulting in less efficient fuel use. Throughout all load conditions, biodiesel blends show higher BSFC than pure diesel, with increases ranging from 8% to 24%. This is primarily due to the lower calorific value of biodiesel, which requires injecting more fuel to achieve the same power output [43]. Among the blends, B15 exhibited the smallest increase in BSFC (8%), indicating superior fuel economy compared to other biodiesel blends, while B25 showed the highest increase (24%), aligning with the findings reported in [44]. This trend implies that increasing the biodiesel content beyond a certain threshold may adversely impact fuel economy due to reduced volatility and higher viscosity.

Incorporation with metallic nano particles specifically Al_2O_3 and TiO_2 into B20 biodiesel has shown a notable reduction in BSFC. This improvement scribed to the nanoparticle's high thermal conductivity and surface area, which enhance the combustion characteristics and heat transfer of fuel air mixture. Al_2O_3 achieved a maximum BSFC reduction of 6.2% at 60% engine load, while TiO_2 exhibited an 8.4% reduction at 40% load relative to B20 blend. Among the combined nanoparticle blends, B20A20T20 (with 20 ppm of each nanoparticle) achieved the highest BSFC

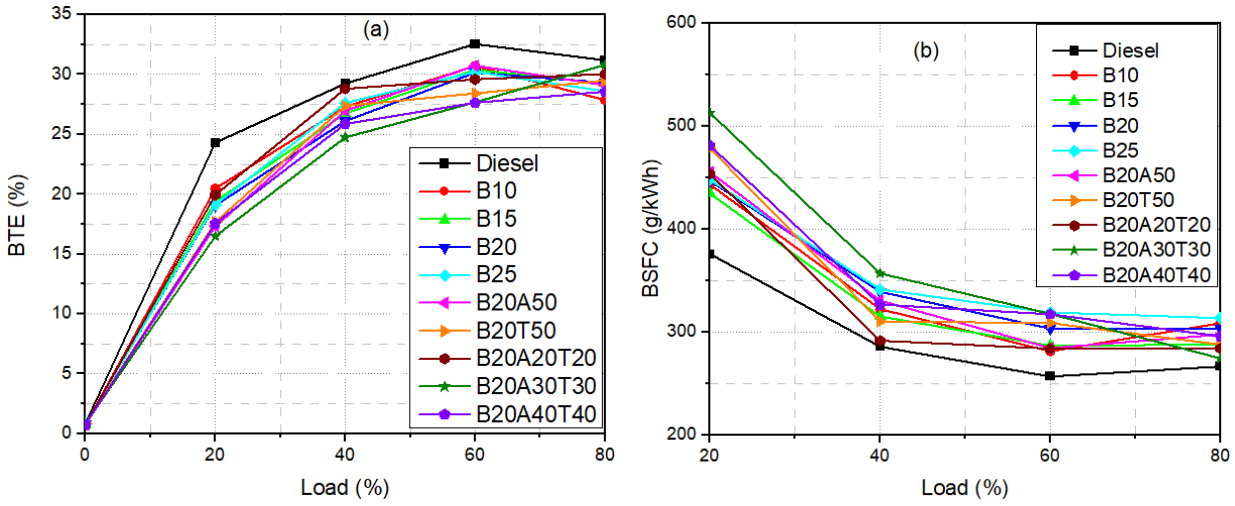
reduction of 13.9%. However, further increases in nanoparticle concentration beyond this point led to a slight rise in BSFC. This may be due to nanoparticle agglomeration at higher concentrations, which can hinder uniform dispersion and reduce combustion enhancement benefits. Therefore, the study identifies a combined concentration of 40 ppm (20 ppm Al_2O_3 + 20 ppm TiO_2) as the optimal dosage for improving fuel economy without negative side effects. Overall, the potential of nanoparticle additives to offset the fuel economy penalty associated with biodiesel, by improving combustion characteristics and reducing BSFC [45].

3.7.3 Exhaust gas temperature

Exhaust Gas Temperature (EGT) is a key indicator of the combustion process within the cylinder, reflecting both combustion completeness and the thermal properties of the fuel. As illustrated in Figure 17 (c), EGT steadily rises with increasing engine load, primarily due to higher fuel injection rates and greater energy release inside the cylinder at elevated loads. Among the fuels tested, pure diesel showed the lowest EGT, while B10 recorded the highest, consistent with findings reported in [46]. This trend reflects the influence of biodiesel's natural oxygen content, which promotes complete combustion and leads to higher flame temperatures. However, literature [47] also indicates that castor oil biodiesel, being rich in unsaturated fatty acid methyl esters (FAMEs), possesses a higher adiabatic flame temperature than diesel, potentially increasing the EGT [48]. Moreover, the elevated cetane number (CN) of biodiesel promotes earlier ignition and extends the fuel's residence time at high temperatures, contributing to higher exhaust gas temperatures (EGT). However, when the biodiesel blend ratio exceeds a certain threshold, EGT tends to decrease. This reduction is likely caused by the increased viscosity and density of the fuel, which hinder proper atomization and combustion efficiency, resulting in lower peak cylinder temperatures and consequently reduced EGT.

The introduction of metallic nanoparticles such Al_2O_3 and TiO_2 into B20 blends demonstrated a notable impact on EGT. Across all load conditions, Al_2O_3 and TiO_2 reduced EGT by approximately 3–8% and 1.6–6.1%, respectively, relative to B20 [49], [50]. This reduction is primarily due to the superior heat transfer and thermal conductivity properties of these nanoparticles, which improve in-cylinder thermal management and enhance combustion stability. Compared to nanobiochar, Al_2O_3 and TiO_2 exhibit better performance due to their ability to dissipate heat more efficiently and catalyze oxidation reactions. Notably, the combined nanoparticle formulation B20A20T20

achieved the highest BSFC reduction of up to 14.3% over B20, outperforming individual nanoparticle additions. This can be explained by the synergistic effect of TiO_2's high specific surface area, which enhances fuel-air mixing, and Al_2O_3's high thermal conductivity, which accelerates flame propagation. However, increasing the nanoparticle concentration beyond the optimal 40 ppm led to increased BSFC and did not yield further EGT reductions, likely due to nanoparticle agglomeration and adverse impacts on fuel flow and atomization. Overall, the inclusion of nanoparticles contributes to a faster combustion rate in the premixed phase, while moderating the heat release during the diffusion-controlled phase, thereby reducing overall EGT [42]. In contrast, a shift in combustion toward the late phase tends to elevate EGT due to prolonged high-temperature residence, as reported in [51]. These results highlight the dual benefit of nanoparticle-enhanced biodiesel blends in improving combustion efficiency while controlling thermal stresses within the engine.



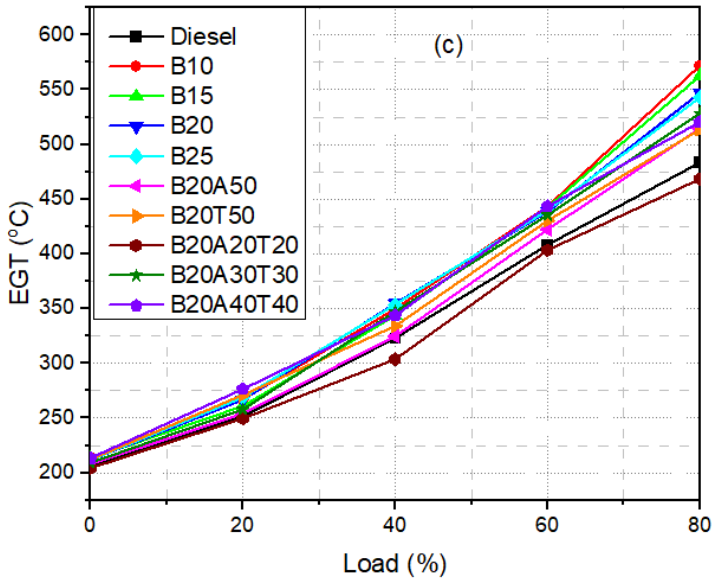


Fig. 17 (a) BTE, (b) BSFC and (c) EGT

3.8 Engine emission Characteristics

3.8.1 NOx emission

The primary factors contributing to the formation of nitrogen oxides (NOx) in diesel engine combustion are high in-cylinder temperatures, elevated Oxygen concentration, and extended fuel duration of stay in the combustion chamber. As depicted in Figure 18 (a), the NOx emission trends for castor biodiesel blends varied significantly with engine load. At no-load conditions, NOx emissions were minimal due to lower combustion temperatures and leaner mixtures. However, as the load increased to 20%, NOx emissions peaked, then declined with further increases in load. This non-linear behavior is linked to changes in combustion temperature and fuel-air equivalence ratio. Under low loads, diesel fuel exhibited lower NOx emissions than biodiesel blends, owing to lower oxygen content and combustion temperatures. However, at higher engine loads, diesel generated greater NOx emissions compared to B15, B20, and B25 blends, primarily due to more complete combustion and elevated in-cylinder temperatures. Biodiesel blends, particularly B10, showed significant increases in Nox ranging from 23% to 116% compared to diesel due to the intrinsic oxygen content of biodiesel, which enhances local combustion temperatures [52]. Conversely, at high load operation, B15 to B25 exhibited up to a 43.2% reduction in NOx emissions relative to diesel, primarily because higher viscosity of biodiesel and the richer air-fuel mixture reduce combustion efficiency and peak temperatures. The trend suggests that although

oxygenated fuels like biodiesel promote NOx formation at moderate loads, they may reduce it under full-load conditions due to incomplete combustion and reduced thermal gradients. Additionally, previous studies [52] suggest that delaying the fuel injection timing can suppress peak combustion temperatures, thereby mitigating NOx formation.

The incorporation of metallic nanoparticles specifically Al_2O_3 and TiO_2 into B20 biodiesel blends revealed a substantial increase in NOx emissions across all load conditions. Al_2O_3 caused an average NOx increase of 86.4%, while TiO_2 led to a 40.2% rise, both compared to base B20. This rise is ascribed to the nanoparticles' superior thermal conductivity, extensive specific surface area, and catalytic activity, which collectively enhance combustion intensity, facilitate better fuel oxidation, and raise in-cylinder temperatures conditions that favor increased NOx formation. Furthermore, the combined use of Al_2O_3 and TiO_2 had high pronounced effect, with B20A30T30 showing highest Rise in NOx levels by 241.5% followed by 155.2% for B20A40T40 and 54.4% for B20A20T20. The synergistic impact of the two nanoparticles results in enhanced combustion efficiency but at the cost of elevated NOx production due to intensified heat release and higher peak temperatures. While nanoparticles effectively reduce BSFC and improve brake thermal efficiency, their role in NOx formation underscores the trade-off between performance and emissions. These findings highlight the need for further strategies, such as exhaust after-treatment systems or injection timing optimization, to control NOx emissions in nanoparticle-enhanced biodiesel combustion systems.

3.8.2 CO emission

The impact of varying castor biodiesel blend ratios on carbon monoxide (CO) emissions is presented in Figure 18 (b), revealing key insights into combustion efficiency across different engine loads. CO shows incomplete combustion, often resulting insufficient oxygen availability, low combustion temperatures, or poor air-fuel mixing. At no-load conditions, CO emissions were observed to be higher due to lean mixtures and lower cylinder temperatures that hinder complete oxidation of CO-to-CO_2. As engine load increased up to 40%, CO emissions declined, reflecting enhanced combustion conditions higher pressure and temperature improve oxidation efficiency. However, beyond a 40% load, CO emissions started to increase again, likely due to the formation of overly rich fuel–air mixtures and higher fuel injection rates, which limit oxygen availability for complete combustion. This pattern is consistent with findings reported in [37], confirming the

typical U-shaped behavior of CO with respect to load. Among the tested fuel blends, B20 demonstrated the lowest carbon monoxide (CO) emissions across all engine load conditions, followed sequentially by B25, B15, and B10. This superior performance of B20 is primarily attributed to the inherent oxygen content in biodiesel, which enhances the oxidation of CO-to-CO_2 during combustion. Notably, B20 achieved a 25–56% reduction in CO emissions across the 0–80% load range compared to conventional diesel. This reduction is credited to biodiesel's oxygenated structure and improved combustion efficiency under varying loads. Furthermore, as the proportion of biodiesel in the blend increases, CO emissions progressively decline, highlighting the role of increased oxygen availability in promoting more complete combustion.

However, inclusion of metallic nanoparticles into B20 led to a counterintuitive rise in CO emissions. TiO_2 increased CO emissions by an average of 4.4%, while Al_2O_3 caused a significantly higher increase of 58% compared to the baseline B20 fuel. Increase of CO with nanoparticle addition can be attributed changes due to fuel properties such as spray characteristics and viscosity, which may have led to poor atomization or uneven combustion under certain operating conditions. Furthermore, the combination of Al_2O_3 and TiO_2 nanoparticles showed even more pronounced effects, with B20A20T20 increasing CO emissions by 17.8%, B20A40T40 by 154.3%, and B20A30T30 by 170.3% compared to B20. These findings suggest that while nanoparticles are often effective in enhancing combustion and reducing BSFC, an excessive concentration can disrupt the combustion process, possibly due to nanoparticle agglomeration, increased viscosity, and altered ignition characteristics. The data imply that 40 ppm may represent the upper threshold for combined nanoparticle concentration in biodiesel blends, beyond which CO emissions significantly worsen. This highlights the importance of optimizing nanoparticle dosage not only for performance gains but also to maintain favorable emission characteristics.

3.8.3 Hydrocarbon emission

In diesel engines, HC result from incomplete combustion processes caused by low cylinder temperatures, insufficient flame propagation, and inadequate injection pressure. As illustrated in Figure 18 (c), HC emissions are highest under no-load conditions due to low combustion temperatures and longer ignition delay (ID), and they gradually decline as engine load increases. This trend is consistent with previously reported findings [53], [54], as increased load enhances in-cylinder temperatures and turbulence, promoting more complete combustion. Among the tested

fuels, pure diesel produced the highest HC emissions, while B10 yielded the lowest. Specifically, HC emissions for B10 were reduced by 55%, followed by 39% for B15, 34% for B20, and 25% for B25 when compared to pure diesel. This reduction is primarily attributed to the oxygenated nature of biodiesel and its higher cetane number, which promote shorter ignition delay, faster combustion, and improved oxidation of hydrocarbons into CO_2 and H_2O. These findings are consistent with those reported in [54], which correlate reduced HC emissions with improved combustion quality in biodiesel blends. The higher HC emissions in pure diesel can be further explained by its longer ignition delay, which allows more time for fuel-air mixing but increases the likelihood of flame quenching and incomplete combustion in low-temperature zones. Additionally, biodiesel's fatty acid composition plays a key role biodiesel with higher levels of unsaturation tends to exhibit lower HC emissions, as unsaturated fatty acids are more reactive and promote better combustion [55]. In contrast, saturated fatty acids with low volatility are prone to incomplete combustion, leading to elevated HC emissions.

The effect of adding metal oxide nanoparticles, specifically Al_2O_3 and TiO_2, to B20 biodiesel was also investigated with a focus on their influence on NOx emissions, which tend to increase with nanoparticle concentration. This rise in NOx is associated with elevated peak cylinder pressure and shortened ignition delay, both of which are intensified by the nanoparticles' capacity to improve heat transfer and speed up combustion process [55]. Nanoparticles possess high surface energy and large surface-to-volume ratios, which contribute to faster and more complete combustion [53], [54]. As a result, while they may reduce HC and CO emissions in some cases by improving oxidation reactions, their presence can significantly raise in-cylinder temperatures thereby increasing NOx formation. The lowest NOx increase was observed with B20T50 at 40.1%, followed by 54% for B20A20T20, 86% for B20A50, 155% for B20A40T40, and the highest, 241% for B20A30T30, all compared to B20. These results suggest a strong trade-off improving combustion efficiency and controlling NOx emissions when using nanoparticles, underscoring the need for optimal nanoparticle dosing and potential emission control strategies such as injection timing optimization or selective catalytic reduction (SCR) to balance performance and environmental impacts.

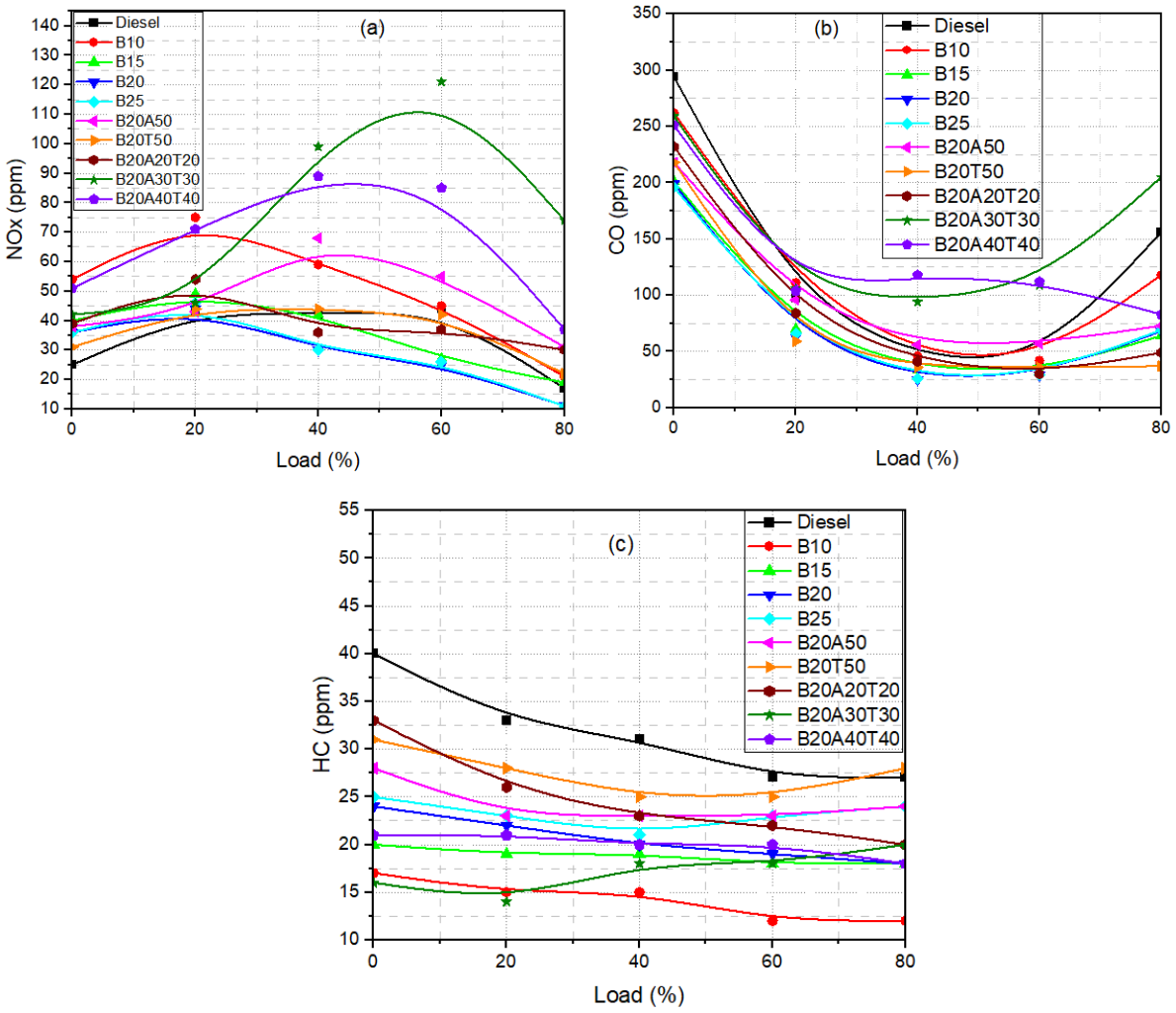


Fig. 18 (a) NOx, (b) CO and (c) HC

4 Conclusion and recommendations

4.1 Conclusions

This study quantitatively evaluated the influence of castor biodiesel and metal oxide nano-additives (Al_2O_3 and TiO_2) on the performance, combustion, and emission characteristics of a single-cylinder CI engine operating at a constant speed of 2700 rpm under varying load conditions (0–80%).

- Biodiesel Production: Castor biodiesel was synthesized via transesterification using a 9:1 methanol-to-oil molar ratio, 1.25 wt% KOH catalyst, and a reaction temperature of 60°C at 650 rpm for 90 minutes. Under these conditions, maximum biodiesel yield was achieved, while further increases in temperature led to catalyst degradation and methanol loss.

- At low loads (0–40%), biodiesel blends exhibited a 5–13% higher heat release rate (HRR) and up to 7.5% higher cylinder pressure (CP) compared to diesel, attributed to enhanced oxygenation and ignition quality. However, at high loads (60–80%), diesel outperformed biodiesel, with HRR exceeding biodiesel by 5–11% due to better atomization and lower viscosity. Nano-additive incorporation (50 ppm each) improved CP by up to 6.3% and HRR by 5.0%, with a synergistic effect observed in the hybrid blend (B20A20T20).
- BTE increased with engine load, peaking at 32.55% for diesel at 60% load. Biodiesel blends (B10–B25) showed 5.6–7.3% lower BTE at full load due to incomplete combustion and higher viscosity. Addition of Al_2O_3 and TiO_2 nanoparticles individually improved BTE by 3.3% and 4.9%, respectively, while the hybrid blend (B20A20T20) achieved a maximum improvement of 10.3% at 40% load. Overdosing nanoparticles reduced BTE by up to 8%.
- Biodiesel blends exhibited 8–24% higher BSFC than diesel, with B25 showing the worst economy. Nano-additive supplementation reduced BSFC by 6.2% (Al_2O_3), 8.4% (TiO_2), and 13.9% for the B20A20T20 hybrid relative to base B20.
- Biodiesel blends showed higher EGT (up to 7.2%) than diesel at low loads due to enhanced oxygen content. At higher loads, blends with higher viscosity showed reduced EGT. Nano-additives lowered EGT by 3–8% (Al_2O_3), 1.6–6.1% (TiO_2), and up to 10.2% for the combined blend, indicating improved combustion and reduced thermal stress.
- Biodiesel blends alone increased NO_x emissions by 23–116%, primarily due to higher combustion temperatures. Nano-additives further elevated NO_x, with Al_2O_3 contributing up to 86.4%, TiO_2 by 40.2%, and the hybrid blend (B20A20T20) peaking at a 241.5% increase indicating a significant trade-off between improved combustion and NO_x control.
- Biodiesel blends reduced CO emissions by 25–56%, but nanoparticle addition led to increased CO emissions up to 58% for individual additives and 170.3% for the hybrid blend, likely due to nanoparticle agglomeration and incomplete oxidation.
- Hydrocarbon emissions were reduced by up to 55%, with B10 showing the best performance. However, nanoparticle use indirectly raised HC levels in some cases due to localized fuel-rich zones from poor dispersion.

Summary: The incorporation of Al_2O_3 and TiO_2 nanoparticles at 50 ppm each into B20 biodiesel significantly improved combustion metrics; yielding up to 10.3% higher BTE and 13.9% lower

BSFC, with EGT reductions of up to 10.2%. However, these performance gains were offset by substantial increases in NO_x emissions (up to 241.5%) and CO emissions (up to 170.3%), underscoring the critical need for optimizing nanoparticle dispersion and dosage. Thus, while nano-enhanced castor biodiesel presents a viable alternative to fossil diesel, careful balancing of performance gains and emission penalties is essential for practical deployment.

4.2 Recommendations

The study concludes that castor biodiesel-nano additive blends are a viable alternative fuel, meeting both ASTM and EN standards for use in diesel engines. The research highlights the significant positive impact of both single and hybrid nanoparticles on fuel characteristics, performance, and emissions. Notably, the B20A20T50 hybrid blend demonstrated substantial improvements in brake power, brake thermal efficiency, torque, and a significant reduction in CO and HC emissions. This is attributed to the enhanced catalytic action and improved fuel oxidation provided by the nanoparticles. The following future directions are recommended to fully harness the potential of castor biodiesel-nanoparticle blends:

- Future research should focus on long-term durability testing to assess engine wear, lubricant degradation, and the effects of nanoparticles on critical components.
- Expanding performance and emissions testing to multi-cylinder engines and higher load conditions will provide a more comprehensive understanding under real-world scenarios.
- Investigations into the long-term stability, dispersion behavior, and potential agglomeration of nanoparticles during storage and engine operation are essential for maintaining fuel consistency.
- Advanced combustion modeling and spray simulation should be employed to optimize nanoparticle-fuel interactions and improve combustion efficiency.
- Additionally, integrating effective after-treatment systems such as SCR or DPF will be crucial to mitigate the elevated NO_x and CO emissions observed with nano-additive use.
- Further work is also needed to explore alternative hybrid nanoparticle combinations and dosing strategies that maximize performance benefits while minimizing emission penalties.

Lastly, environmental impact studies should evaluate the fate of unburned nanoparticles in exhaust emissions to ensure safe and sustainable deployment.

By addressing these areas, the potential of castor biodiesel-nano additive blends can be more fully realized as a sustainable, high-performance alternative to conventional diesel fuels.

Contributions

Yordanos Geremew Chernet: Conceptualization, Methodology, Validation, Writing - Original Draft**; Samson Mekbib Atnaw:** Supervision, Project Management, Visualization, Writing - Review & Editing, Validation**; Adem Siraj Mohammed:** Supervision, Writing - Review & Editing**.**

Declarations

Funding: This research was funded by the Sustainable Energy Center of Excellence, Addis Ababa Science and Technology University, Addis Ababa, Ethiopia. Grant No. IGP 20/2024.

Data Availability Statement: The data presented in this study are available from the corresponding author upon reasonable request.

Acknowledgments: Access to the experimental facilities granted at the Jimma Institute of Technology is gratefully acknowledged.

Conflicts of Interest: The authors declare no conflicts of interest in this work.

Ethics approval and consent to participate: Not applicable since there were no human or animal subjects. All authors listed on the title page have contributed significantly to the work.

Consent for publication: All authors agree to the submission of the manuscript to Discover Applied Sciences.

Clinical Trial Registration: Not applicable. This study is not a clinical trial and is therefore not registered in a clinical trial registry.

References

[1] M. D. Ali, S. M. Atnaw, and A. S. Mohammed, “Experimental Investigation of the Performance and Emission Characteristics of Methanol-Ethanol gasoline Blending With Iso-Butanol Additive on the Spark-Ignition Engine,” *Platf. A J. Eng.*, vol. 6, no. 3, p. 2,

2022, doi: 10.61762/pajevol6iss3art20022.

[2] U. Shahzad, “ITEE Journal The Need For Renewable Energy Sources,” *Energy*, vol. 2, pp. 0–2, 2001.

[3] E. A. El Shenawy *et al.*, “Investigation and performance analysis of water-diesel emulsion for improvement of performance and emission characteristics of partially premixed charge compression ignition (PPCCI) diesel engines,” *Sustain. Energy Technol. Assessments*, vol. 36, no. September, p. 100546, 2019, doi: 10.1016/j.seta.2019.100546.

[4] H. R. and M. Roser, “Air Pollution.pdf.” Our World in Data, p. 14, 2021.

[5] M. A. Islam, M. Hasanuzzaman, N. A. Rahim, A. Nahar, and M. Hosenuzzaman, “Global renewable energy-based electricity generation and smart grid system for energy security,” *Sci. World J.*, vol. 2014, 2014, doi: 10.1155/2014/197136.

[6] D. Sakthivadivel, P. Ganesh Kumar, R. Prabakaran, V. S. Vigneswaran, K. Nithyanandhan, and S. C. Kim, “A neem oil-based biodiesel with DEE enriched ethanol and Al2O3nano additive: An experimental investigation on the diesel engine performance,” *Case Stud. Therm. Eng.*, vol. 34, no. February, p. 102021, 2022, doi: 10.1016/j.csite.2022.102021.

[7] K. S. Khoo, I. Ahmad, K. W. Chew, K. Iwamoto, A. Bhatnagar, and P. L. Show, “Enhanced microalgal lipid production for biofuel using different strategies including genetic modification of microalgae: A review,” *Prog. Energy Combust. Sci.*, vol. 96, no. December 2022, p. 101071, 2023, doi: 10.1016/j.pecs.2023.101071.

[8] L. Canoira, J. García Galeán, R. Alcántara, M. Lapuerta, and R. García-Contreras, “Fatty acid methyl esters (FAMEs) from castor oil: Production process assessment and synergistic effects in its properties,” *Renew. Energy*, vol. 35, no. 1, pp. 208–217, 2010, doi: 10.1016/j.renene.2009.05.006.

[9] A. Taheri-Garavand, A. Heidari-Maleni, T. Mesri-Gundoshmian, and O. D. Samuel, “Application of artificial neural networks for the prediction of performance and exhaust emissions in IC engine using biodiesel-diesel blends containing quantum dot based on carbon doped,” *Energy Convers. Manag. X*, vol. 16, no. May, p. 100304, 2022, doi:

10.1016/j.ecmx.2022.100304.

[10] A. Sharma, Shadiya, T. Sharma, R. Kumar, K. Meena, and S. S. Kanwar, “Biodiesel and the Potential Role of Microbial Lipases in Its Production,” *Microorg. Sustain.*, vol. 17, no. September, pp. 83–99, 2019, doi: 10.1007/978-981-13-8844-6_4.

[11] S. T. Keera, S. M. El Sabagh, and A. R. Taman, “Castor oil biodiesel production and optimization,” *Egypt. J. Pet.*, vol. 27, no. 4, pp. 979–984, 2018, doi: 10.1016/j.ejpe.2018.02.007.

[12] K. Kalaimurugan, S. Karthikeyan, M. Periyasamy, and G. Mahendran, “Combustion studies on CI engine with cerium oxide nanoparticle added neochloris oleoabundans biodiesel-diesel fuel blends,” *Mater. Today Proc.*, vol. 33, no. xxxx, pp. 2886–2889, 2020, doi: 10.1016/j.matpr.2020.02.779.

[13] M. E. M. Soudagar, N. N. Nik-Ghazali, M. Abul Kalam, I. A. Badruddin, N. R. Banapurmath, and N. Akram, “The effect of nano-additives in diesel-biodiesel fuel blends: A comprehensive review on stability, engine performance and emission characteristics,” *Energy Convers. Manag.*, vol. 178, no. October, pp. 146–177, 2018, doi: 10.1016/j.enconman.2018.10.019.

[14] P. Dimitriou and T. Tsujimura, “A fully renewable and efficient backup power system with a hydrogen-biodiesel-fueled IC engine,” *Energy Procedia*, vol. 157, no. 2018, pp. 1305–1319, 2019, doi: 10.1016/j.egypro.2018.11.296.

[15] S. N. A. Yusof, N. A. C. Sidik, Y. Asako, W. M. A. A. Japar, S. B. Mohamed, and N. M. az Muhammad, “A comprehensive review of the influences of nanoparticles as a fuel additive in an internal combustion engine (ICE),” *Nanotechnol. Rev.*, vol. 9, no. 1, pp. 1326–1349, 2021, doi: 10.1515/ntrev-2020-0104.

[16] Ü. Ağbulut, M. Karagöz, S. Sarıdemir, and A. Öztürk, “Impact of various metal-oxide based nanoparticles and biodiesel blends on the combustion, performance, emission, vibration and noise characteristics of a CI engine,” *Fuel*, vol. 270, no. January, 2020, doi: 10.1016/j.fuel.2020.117521.

[17] J. Gardy, A. Hassanpour, X. Lai, M. H. Ahmed, and M. Rehan, “Biodiesel production from used cooking oil using a novel surface functionalised TiO2 nano-catalyst,” *Appl. Catal. B Environ.*, vol. 207, pp. 297–310, 2017, doi: 10.1016/j.apcatb.2017.01.080.

[18] D. C. Gosai, A. J. Modi, and A. K. Gillawat, “Impact of Nano-Fuel Additives and Nano-Lubricant Oil Additives on Diesel Engine Performance and Emission Characteristics,” *J. Heat Mass Transf. Res.*, vol. 12, no. 1, pp. 103–122, 2025, doi: 10.22075/JHMTR.2024.33460.1531.

[19] S. K. FASOGBON and S. O. OYEDEPO, “Nano-additive blends examination of performance and emission profile of CI engines fuelled with waste cooking oil based-biodiesel,” *J. Therm. Eng.*, vol. 11, no. 1, pp. 1–15, 2025, doi: 10.14744/thermal.0000899.

[20] H. L. Allasi, A. J. Selvam, M. V. Soosaimariyan, and S. J. Arul, “Enhancing diesel engine efficiency with waste cooking oil biodiesel and nano additives for sustainable fuel applications,” *Sci. Rep.*, vol. 15, no. 1, pp. 1–17, 2025, doi: 10.1038/s41598-025-17528-7.

[21] J. M. Avramovic *et al.*, “Castor Oil Extraction: Methods and Impacts,” *Sep. Purif. Rev.*, vol. 54, no. 1, pp. 60–82, 2025, doi: 10.1080/15422119.2024.2361674.

[22] R. Naveenkumar and G. Baskar, “Process optimization, green chemistry balance and technoeconomic analysis of biodiesel production from castor oil using heterogeneous nanocatalyst,” *Bioresour. Technol.*, vol. 320, p. 124347, 2021, doi: 10.1016/j.biortech.2020.124347.

[23] A. S. Mohammed, V. R. Ancha, S. M. Atnaw, M. Desta, and R. Bhandari, “Analysis of Cylinder Pressure and Heat Release Rate Variation in Diesel Engine Fueled with Croton Macrostachyus (CMS) Seed Oil Biodiesel as an Alternative Fuel,” *Energies*, 2025, doi: 10.3390/en18061449.

[24] A. Moreno and M. H. Sipponen, “Overcoming Challenges of Lignin Nanoparticles: Expanding Opportunities for Scalable and Multifunctional Nanomaterials,” *Acc. Chem. Res.*, vol. 57, no. 14, pp. 1918–1930, 2024, doi: 10.1021/acs.accounts.4c00206.

[25] W. Guo, X. Cao, D. Tan, B. Wulan, J. Ma, and J. Zhang, “Thermal-Driven Dispersion of

Bismuth Nanoparticles among Carbon Matrix for Efficient Carbon Dioxide Reduction," *Angew. Chemie - Int. Ed.*, vol. 63, no. 28, 2024, doi: 10.1002/anie.202401333.

[26] A. Siraj Mohammed, V. Ramaya Ancha, and S. Mekbib Atnaw, "Optimization of biodiesel production from Croton Macrostachyus seed oil with calcium oxide (CaO) catalyst and Characterization: Potential assessment of seed and kernel," *Energy Convers. Manag. X*, vol. 24, no. October, 2024, doi: 10.1016/j.ecmx.2024.100791.

[27] Q. Zhang *et al.*, "Advancements in Nanomaterial Dispersion and Stability and Thermophysical Properties of Nano-Enhanced Phase Change Materials for Biomedical Applications," *Nanomaterials*, vol. 14, no. 13, 2024, doi: 10.3390/nano14131126.

[28] V. Ávila Vázquez, R. A. Díaz Estrada, M. M. Aguilera Flores, C. Escamilla Alvarado, and H. C. Correa Aguado, "Transesterification of non-edible castor oil (Ricinus communis L.) from Mexico for biodiesel production: a physicochemical characterization," *Biofuels*, vol. 11, no. 7, pp. 753–762, 2020, doi: 10.1080/17597269.2020.1787700.

[29] D. Kumar, A. Kumar, A. Singla, and R. Dewan, "Production and tribological characterization of castor based biodiesel," *Mater. Today Proc.*, vol. 46, no. xxxx, pp. 10942–10949, 2021, doi: 10.1016/j.matpr.2021.02.009.

[30] M. Tesfaye Lamore, D. Seyoum Zeleke, and B. Yitayew Kassa, "A Comparative Study on the Effect of Nano-additives on Performance and Emission Characteristics of CI Engine Run on Castor Biodiesel Blended Fuel," *Energy Convers. Manag. X*, p. 100493, 2023, doi: 10.1016/j.ecmx.2023.100493.

[31] R. B. Vieira *et al.*, "Oxidative Stability and Molecular Reactivity of Biodiesel from Castor and Cottonseed Oil Blends by Homogeneous and Heterogeneous Catalysis," *Energy Technol.*, vol. 2500287, pp. 1–15, 2025, doi: 10.1002/ente.202500287.

[32] O. R. Obanla, F. U. Mohammed, O. S. Alebiosu, M. E. Ojewumi, T. E. Oladimeji, and D. E. Babatunde, "Study on the Lubricating Properties of Castor (Ricinus communis) and Hydroxylated Rubber (Hevea brasiliensis) Seed Oil," *ACS Omega*, vol. 6, no. 43, pp. 28471–28476, 2021, doi: 10.1021/acsomega.0c05810.

[33] D. Balasubramanian and K. R. Lawrence, “Influence on the effect of titanium dioxide nanoparticles as an additive with Mimusops elengi methyl ester in a CI engine,” *Environ. Sci. Pollut. Res.*, pp. 16493–16502, 2019.

[34] M. I. Kandil, H. S. Jahin, H. A. Dessouki, and M. Y. Nassar, “Synthesis and characterization of γ-Al2O3 and α-Al2O3 nanoparticles using a facile, inexpensive auto-combustion approach,” *Egypt. J. Chem.*, vol. 64, no. 5, pp. 2509–2515, 2021, doi: 10.21608/EJCHEM.2021.61793.3330.

[35] C. Chinglenthoiba, A. Das, and S. Vandana, “Enhanced biodiesel production from waste cooking palm oil , with NaOH-loaded Calcined fish bones as the catalyst,” *Environ. Sci. Pollut. Res.*, 2020.

[36] J. Huang, Y. Zou, M. Yaseen, H. Qu, R. He, and Z. Tong, “Fabrication of hollow cage-like CaO catalyst for the enhanced biodiesel production via transesterification of soybean oil and methanol,” *Fuel*, vol. 290, no. November 2020, p. 119799, 2021, doi: 10.1016/j.fuel.2020.119799.

[37] A. Turab, M. Ali, H. Ajab, N. Abbas, U. Sajjad, and K. Hamid, “Influence of nano additives on Diesel-Biodiesel fuel blends in diesel engine : A spray , performance , and emissions study,” *Energy Convers. Manag. X*, vol. 23, no. March, p. 100574, 2024, doi: 10.1016/j.ecmx.2024.100574.

[38] T. Sathish, J. Giri, R. Saravanan, R. Zairov, and S. M. M. Hasnain, “Nano-fuels of Al 2 O 3 / SiO 2 / MgO / tamarind seed oil biodiesel for CI engines : An evaluation of combustion consumption and emission performance,” *Int. J. Thermofluids*, vol. 23, no. August, p. 100815, 2024, doi: 10.1016/j.ijft.2024.100815.

[39] Z. Sun, H. Van Beers, M. Cuijpers, B. Somers, and N. Maes, “Design of experiments optimized OMEx-diesel blends on a heavy-duty engine − Part 1: Combustion and emissions analysis with EGR and injection timing variation,” *Fuel*, vol. 381, no. PA, p. 133392, 2025, doi: 10.1016/j.fuel.2024.133392.

[40] L. Razzaq *et al.*, “Engine performance and emission characteristics of palm biodiesel blends with graphene oxide nanoplatelets and dimethyl carbonate additives,” *J. Environ. Manage.*,

vol. 282, no. December 2020, p. 111917, 2021, doi: 10.1016/j.jenvman.2020.111917.

[41] L. Razzaq *et al.*, "Effect of biodiesel-dimethyl carbonate blends on engine performance, combustion and emission characteristics," *Alexandria Eng. J.*, vol. 61, no. 7, pp. 5111–5121, 2022, doi: 10.1016/j.aej.2021.10.015.

[42] M. S. Gad, B. M. Kamel, and I. Anjum, "Improving the diesel engine performance , emissions and combustion characteristics using biodiesel with carbon nanomaterials," *Fuel*, no. July, p. 119665, 2020, doi: 10.1016/j.fuel.2020.119665.

[43] A. Alahmer *et al.*, "Modeling and Optimization of a Compression Ignition Engine Fueled with Biodiesel Blends for Performance Improvement," *Mathematics*, vol. 10, no. 3, 2022, doi: 10.3390/math10030420.

[44] A. Babji, G. Rambabu, B. Naik, D. Levi, P. Cheworei, and D. S. Rao, "Optimization of Compression Ignition Diesel Engine Combustion , Emission , and Performance Characteristics at Higher Blends of Biodiesel Using RSM," *Process Integr. Optim. Sustain.*, pp. 953–973, 2024, doi: 10.1007/s41660-024-00407-5.

[45] L. Rao, S. Kaur, S. Vara, P. Lankapalli, and J. Sagari, "Effect of multi ferrites nanoparticles added Terminalia bellirica biodiesel on diesel engine : Combustion , performance , and emission studies," *Int. J. Thermofluids*, vol. 22, no. April, p. 100652, 2024, doi: 10.1016/j.ijft.2024.100652.

[46] G. Saravanan and P. Thiyagarajan, "Performance , combustion and emission parameters of Scenedesmus obliquus methyl ester in single - cylinder CI engine : an experimental study," *J. Therm. Anal. Calorim.*, vol. 149, no. 23, pp. 14325–14341, 2024, doi: 10.1007/s10973-024-13729-w.

[47] A. M. A. Attia, A. R. Kulchitskiy, M. Nour, A. I. El-seesy, and S. A. Nada, "The influence of castor biodiesel blending ratio on engine performance including the determined diesel particulate matters composition," *Energy*, vol. 239, p. 121951, 2022, doi: 10.1016/j.energy.2021.121951.

[48] H. A. Dhahad, M. A. Fayad, M. T. Chaichan, A. Abdulhady, and T. Megaritis, "Influence

of fuel injection timing strategies on performance , combustion , emissions and particulate matter characteristics fueled with rapeseed methyl ester in modern diesel engine," *Fuel*, vol. 306, no. X, p. 121589, 2021, doi: 10.1016/j.fuel.2021.121589.

[49] A. Murtaza, L. Ali, M. T. Ghannam, and M. Y. E. Selim, "Impact of biodiesel blended fuel with nanoparticles on performance and noise emission in compression ignition engine," *Int. J. Thermofluids*, vol. 19, no. June, p. 100390, 2023, doi: 10.1016/j.ijft.2023.100390.

[50] M. Elkelawy, E. Shenawy, A. El Shenawy, H. A. Bastawissi, and M. M. Shams, "Impact of Carbon Nanotubes and Graphene Oxide Nanomaterials on the Performance and Emissions of Diesel Engine Fueled with Diesel / Biodiesel Blend," *processes*, 2023.

[51] A. R. Adib, M. Rahman, T. Hassan, M. Ahmed, and A. Al Rifat, "Novel biofuel blends for diesel engines : Optimizing engine performance and emissions with C . cohnii microalgae biodiesel and algae-derived renewable diesel blends," *Energy Convers. Manag. X*, vol. 23, no. August, p. 100688, 2024, doi: 10.1016/j.ecmx.2024.100688.

[52] C. Jit *et al.*, "Improving the combustion and emission performance of a diesel engine powered with mahua biodiesel and TiO 2 nanoparticles additive," *Alexandria Eng. J.*, vol. 72, pp. 387–398, 2023, doi: 10.1016/j.aej.2023.03.070.

[53] A. M. A. Attia, M. Nour, A. I. El-seesy, and S. A. Nada, "The effect of castor oil methyl ester blending ratio on the environmental and the combustion characteristics of diesel engine under standard testing conditions," *Sustain. Energy Technol. Assessments*, vol. 42, no. October, p. 100843, 2020, doi: 10.1016/j.seta.2020.100843.

[54] M. A. Fayad and H. A. Dhahad, "Effects of adding aluminum oxide nanoparticles to butanol-diesel blends on performance , particulate matter , and emission characteristics of diesel engine," *Fuel*, vol. 286, no. P2, p. 119363, 2021, doi: 10.1016/j.fuel.2020.119363.

[55] K. Masera, A. K. Hossain, and G. Griffiths, "Achieving biodiesel standards through saturation level optimisation," *Front. Fuels*, vol. 3, no. March, 2025, doi: 10.3389/ffuel.2025.1528451.